Universitat Politècnica de Catalunya

Thesis submitted for Master's degree in Numerical Methods

Inverse Analysis of Hybrid Cell-centered/Vertex Model

Author: Malik Ali A. Dawi

Supervisor: José Javier Muñoz Romero

Abstract

Mechanical forces plays a crucial role in coordinating morphogenesis. In this work we preform inverse analysis in order to infer cellular contractions from a dataset of observed deformations. We proceed in the framework of vertex models which is one of the most commonly used descriptions for cell monolayer. We have found that inverting mechanical equilibrium arises various challenges regarding uniqueness and boundary condition. Furthermore, we have particularized our analysis, to deduce the contraction that mediates epithelial wound closure, using microscopic images of *Drosophila* embryo.

Acknowledgement

The author sincerely thanks Professor José Muñoz for his continuous help and support.

Contents

Chapter 1

Introduction

1.1 Overview

Mechanical forces are essential part of many of cellular processes. For many years, researchers have been studying the factors that govern development and diseases, putting their main foucse on factors such as genies, chemicals and hormones. A growing body of studies have shown that the mechanical interaction in cellular level is equally important. Evidence have revealed that cell-cell and matrix-cell interchange of physical forces plays a crucial role in regulating many of development stages [1], along with many other physiological and pathological process including wound healing [2], angiogenesis [3], cancer metastasis [4] [5].

Morphogenetic processes has been a fundamental example on the integration of mechanical froces with biochemical processes. The processes by which a multicellular organism is developed typically involve dramatic changes in cell number, size, shape and position, these changes arise from well known cellular activities such as,*cell proliferation death, metabolic growth, cell elongation and cell migration.* An essential feature for all these processes to reflect a global changes on tissue level, is the generation of internal forces by molecular motors along with their transmission via intercellular junctions [6]. A classical example for such coordinated behaviuor, is the contractile activity at the apical surface of epithelial cells, which triggers tissue folding and invagination during the development of *Drosophila* embryos [7]. Deep understanding of such morphogenetic processes requires deciphering how forces are being generated on an individual cell basis, how those forces are being transmitted between cells, as well as how they are integrated globally to trigger changes in tissue/organism level.

One of main challenges in analyzing the role of forces in morphogenesis is the fact that the mechanical behavior need to be sensed and monitored in nanoscopic framework. Rescently, there has been significant advances in image acusiation tools, which have provided live *in-vivo* images with high spatial and temporal resolutions. Such developemts have made it feasible to observe and track dynamical changes in cells and tissues. In

addition, several biopysical techniques such lazer ablation and micropipettes have given deeper insight into the processes by which forces are generated and propagated within cells and tissues, e.g. [8] [9].

More broadly, the role of cell-generated forces is not only restricted to driving morphogenesis but also, it is realized as the coordinator that establish *homeostasis* both inside individual cells and within the mechanically coupled tissue and organ . In fact, cells have the ability to sense changes in force equilibrium, whether it is due to environmental influences or internal contractions. And these mechanical signals are transduced into changes in biochemistry and gene expression at molecular level, a mechanism that is well known as *mechanotrnsduction* [10] [11]. It implies that cellular signaling can be altered through mechanosensing and thereby switch cells between different fates (e.g., growth, differentiation, motility) by changing force distributions, modulating cell shape, and activating specific mechanotransduction pathways [12]. Then when it comes to development control or maintaining the homestasis of adult organ, they are now perceived as mechanochemical processes, in which intracellular signals generated by mechanosensation response can feed back to alter internal force generation, and this feedback loop appears to be the main conductor for self-organizing phenomena [13].

The growing role of mechanical forces in biology imposes the possibility that a better understanding of mechanotrnsduction patterns might increases the chances of reversing developmental defects for treating diseases, such as cancer, by restoring normal mechanical loading conditions or by correcting abnormal mechanochemical signaling mechanisms [14].

1.2 Cell Mechanics

Studies of cell mechanics over the last years have given a novel phenomenological insight into the rheologically of cells, such that it dependents upon cell type, loading protocol and loading frequency. Undoubtedly, evaluating cellular elasticity and viscosity provide valuable information for comparative characterization between different treatments, however, the mechanical behavior of the cell is inherently much more complicated. Due to the heterogeneity and complexity of the cell and the cytoskeleton, submicrometer-scale measurements can lead to considerably different evaluations of mechanical properties compared to bulk (several micrometer-scale) measurements.

In spite of the structural and dynamical complexity of cells, experiments has establish four phenomenological laws that are universal and apply among all cell types [15]. First, cell rheology is scale-free; meaning that there is no characteristic relaxation times determine the dynamics of the cytoskeletal matrix, rather, relaxation times are distributed as a power law. Secondly, cells are prestressed; mechanical stresses are continuously generated, mainly by myosin motors. Third, the fluctuationdissipation theorem breaks down

and diffusion is anomalous. And Lastly, stiffness and dissipation are altered by stretch; the rheological properties and characteristic of cells are perturbed when they are subjected to mechanical loading. The coexistence of various passive and active mechanisms inside cells have arisen discrepancies on their respond to mechanical loading, showing different behaviors, including stiffening , rejuvenation and fluidization[16] [17] [18].

One of the main ongoing challenges in the field of cell mechanics is to find a unified framework under which the measured phenomenological behaviors can be interpreted to obtain realistic information about the dynamics of the microstructure of the cell, or vice versa to estimate the bulk rheological properties from the observed microstructural interactions. The majority of the work to date considers a top-down strategy, using viscoelastic rheological models (springs and dashpots). The combination of several springs and dashpots in serial or parallel (e.g. Maxwell model [19], Kelvin-Voigt model [20]) leads to exponential decay functions that provides a good fits to the experimental relaxation data. On the other hand, others consider down-top rheology based on the microstructure of the cell, such as, porous-based rheological model for fluidisation [21]. However there is still no clear mechanistic theory to explain the physical mechanisms that govern the universal cellular behaviors and encompasses such rich phenomenological behavior.

1.3 Computational Approaches

One-cell-thick monolayer is the most basic tissue in multicelular organism, typically the are constructed by an aggregation of cells which are coupled to one another by intercellular junctions. Cells within monolayers are able to produce forces through microtubule polymerization or osmotic pressure, however, force generation relies highly on the activities of motor proteins, such as myosins [22]. These proteins along with actin filaments represent the contractile unit that introduce changes to cytoskeletal structures, deformations are then transmitted to neighboring cells and the extracellular environment via adherens junctions, Figure 1.1 shows typical examples of force generation in epithelium.

Furthermore, it has been well established that cortical tension due to actin-myosin contractility and its transmission are two conservative properties, which has motivated researchers to apply mechanical principles such as force equilibrium and minimal energy in order to model tissue self-organization [23]. In literature, we can see a huge step in this direction, involved the development of several types of computational approaches. Generally, these models can be classified into two categories: continuum models and cell-based models [6] [24] [25].

Continuum Models along with finite element methods have been extensively used to describe biological processes in tissue level. These models tend to be very appealing when it comes to achieving an engineering-like-material response, allowing more free-

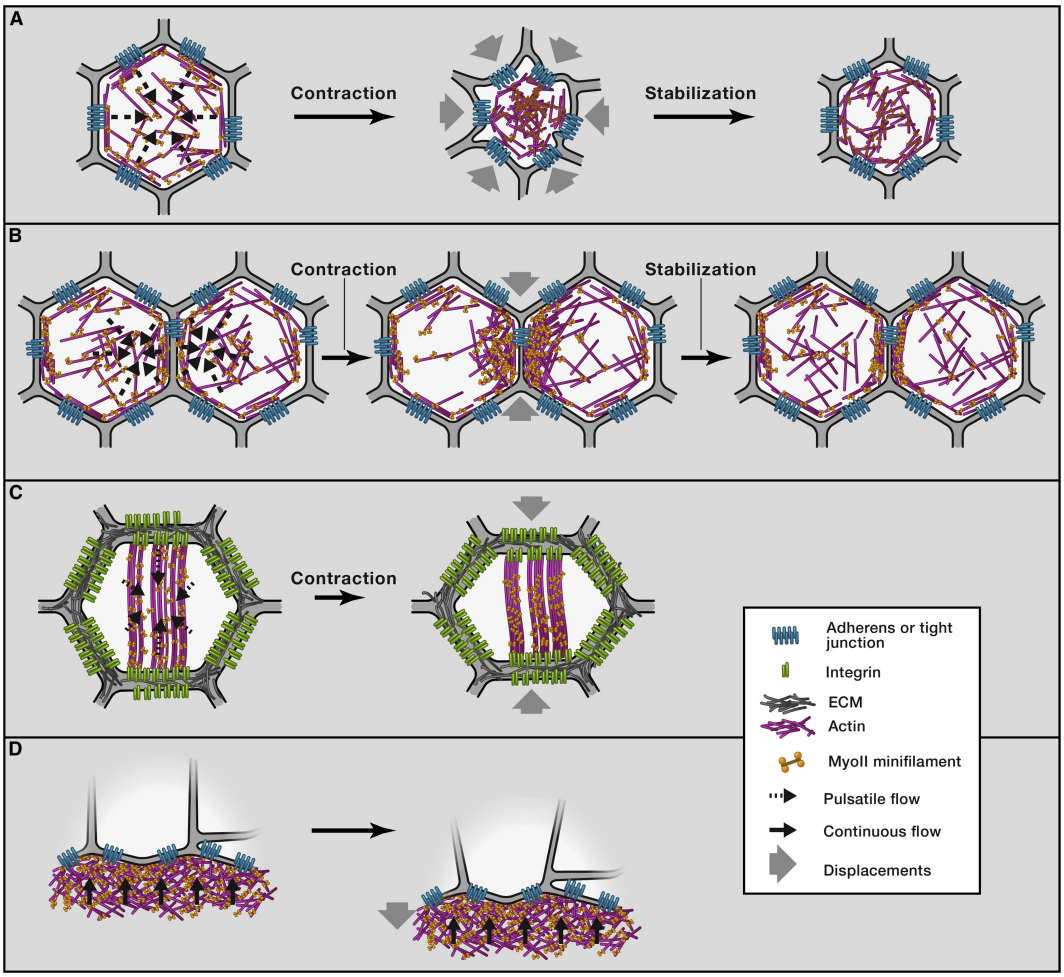

Figure 1.1: Actin-Myosin Network Dynamics and Force Generation [6].

(A) Once coupled to adhesive contacts, pulsatile and centripetal flow of the apical actin-myosin network promotes apical cell constriction.

(B) Pulsatile anisotropic flow induces junction shortening during cell intercalation. Resultant enrichment of actin-myosin at the junction stabilizes junction length reduction.

(C) Basal myosin flow on a static-oriented actin network produces anisotropic deformation of the base of the Drosophila follicular cells.

(D) Continuous actin-myosin flow in the zebrafish yolk cell produces the mechanical force necessary for EVL spreading over the yolk cell during early zebrafish development.

dom to exploit constitutive laws of continuum mediums as well as producing nonlinear behaviors. An application of such models can be found in the study of morphologies of biological tubes [26], which involved describing the mechanical instabilities of a single layer of epithelial cells when it is affected by various pathologies. The complex pattern of mprophgentic processes always requirs major modifications to the generic FE formulation. For instance, active strains are introduced to describe cellular contractions in the simulation of the bucking phenomenon (ventral furrow invagination, Figure 1.2, during the development of *Drosophila* embryos [27] [28]. Correspondingly, we can find an extension of the classical continuum mechanics equations that provided computational framework for growth and remodeling in tissues [29].

However, using FE approach is very challenging when it comes to taking into account cell arrangement and keeping track of cell-cell boundaries, special algorithms need to be implemented to overcome cell neighbor changes considering more sophisticated re-meshing techniques [30]. Besides, since continuum models treat the individual cell and its adhesion in an averaged sense, it become very complex to include subcelluar processes such protein activities and signaling pathways.

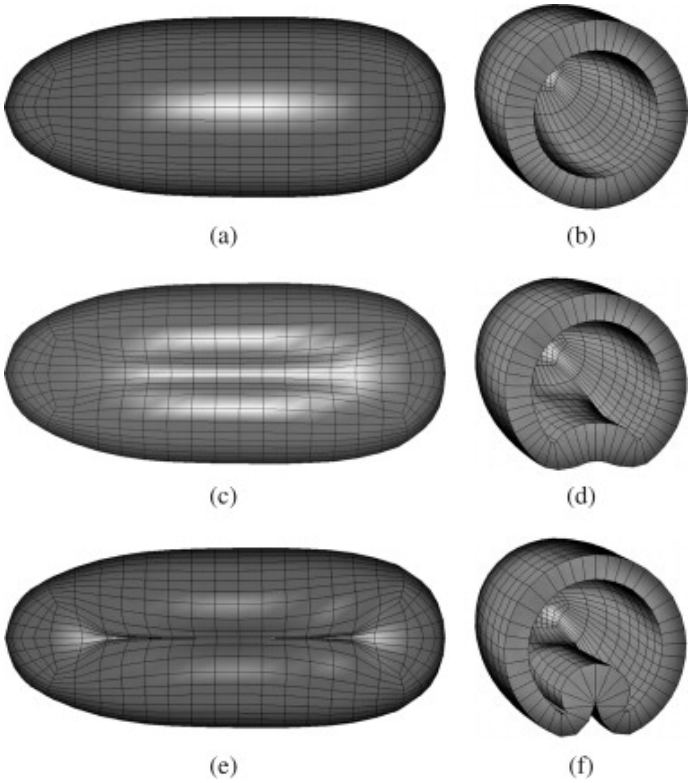

Figure 1.2: Series of deformations during the invagination of Drosophila embryo [28].

Discrete Models: The other family of models is based on discrete approaches, in which cell population is explicitly presented by an aggregation of individual cells. The characteristics of one cell varies between different approaches, but normally they include information about the microscopic state (e.g. position, velocity, boundary, internal biological state), therefore, they allow more freedom to obtain realistic behavior by incorporate cellular process (motility, mitosis, apoptosis). One of the earliest models of this type is cellular automaton model (CA), where the computational domain is discretized into fixed lattice on which cells can occupy sites [31]. Although this model has been very successful in describing proliferation and growth with an efficient cost, the laws of motion are replaced with simplified rules making it very difficult to include rigid body motions or mechanical deformation [32]. Another class of this type of models is cellular Potts model (CP), here cells are considered to occupy several lattice sits providing more realist representation of cell shapes. The motion of cells in CP models is governed by energy minimization, where mechanical details such cell membrane tension and cell-adhesion can be incorporated [33]. Unlike CA models these type of models are computationally more intensive, as Monte Carlo algorithms are commonly used as minimization tool, they are more suitable for a small population of cells [34].

Vertex Models (VM), most of all, have gained more acceptance, when it comes to investigating the dynamics of epithelial tissues. In this model epithelial sheets are described as a set of polygonal cells with vertices and edges shared among neighboring cells, such that the kinmatices of a single cell (e.g. volume and cellular interface) as well as the whole tissue are defined by the position of vertices. The realistic representation of cell shapes and more improtnatly their explicit coupling, have made this model a successful candidate in various applications [35] [36]. One of the key component of VMs is their ability to incorporate cell neighbor rearrangements within an epithelial sheet, there are several biological processes which have been well described by VMs, including, growth of epithelial monolayer [37] [38], gastrulation in *Drosophila* [39] [40], wound healing [41] [42], cone photoreceptor organization on Zebrafish [43].

Practically, we can find that VMs are implemented in variuos ways, of course, depending on the application which they serve, although the principle is very similar. It based on introducing an effective energy that depends on the motion of vertices, and the mechanical equilibrium of tissue is considered as the minimal of such an energy. Such that, the collective motion and deformation of the epithielial tissue and its constitutive cells are obtained by minimizing the energy with respect to the position of vertices [37]-[43]. There has been slight differences on definition of the total energy, but normally they implicate two main aspects. Firstly, an elastic potential resembling the elasticity of epithelial sheet, in which cells can store energy due to changes in cell perimeter, area 2D/volume 3D. And Secondly, a work done by active forces, resembling the contractility of cells, which are normally defined as line tension between two vertices or/and as contraction of cell perimeter [36] [38] [42].

As morphogenetic processes involve the deformation of tissues in time, with cells showing highly dynamic behavior [23], several approaches have been proposed to describe the dynamics of vertices. One way is to consider a quasi-static approach in which tissue is assumed to relax instantly to the closest mechanical equilibrium (minimal-energy), and the temporal deformation is described by viscoelastic constitutive law [44] [42]. While others hypothesize that the motion of vertices is overdamped, instead they explicitly consider a dissipative force acting on vertices [38] [45]. Eventually, since both approaches assume that inertia is negligible, they both lead to first-order ODE describing the dynamical behavior of the tissue.

For more accurate description of epithelial dynamics, cells must be allowed to form/break bonds, divide and rearrange neighbors. This type of process are introduced to the context of VMs by changes in connectivity among vertices, with variety of rules and operation to control these changes (e.g. see [35] [36] [42] [45]). The evolution of the system is thus a combination of relaxation to mechanical equilibrium and changes in tissue connectivity according to the prescribed cell rearrangement processes.

Apparently, we can anticipate that vertex models will play an important role in the future to gain a deeper understanding of how forces generated inside cells affect the shape and mechanics of epithelial sheets. The appearance of new experimental methods that allow for imaging of epithelial morphogenesis with high resolution in time and space will open new frontiers in the application of vertex models to relevant biological questions.

1.4 Force Measurement and Inverse Analysis

In contrast to common engineering material such metals and plastic, cells and tissues are considerably soft objects. The ability to preform mechanical tests or measure forces with accurate length scales has only been possible after recent advancements in surface sciences. For instance, the introduction of piezoelectric ceramics which can change shape in nanometer level increments, or the microfabrication of micron-size cantilevers and mechanical parts. These tools had configured various measuring techniques which can be used to apply controlled deformations and forces on cells, such as magnetic bead cytometry [46], optical tweezers [47], cell/tissue stretchers [48] [49] and Atomic force microscopy (AFM) [50].

Another class of experimental techniques, which are those that monitor the ability of a cell to generate forces. Traction Force Microscopy (TFM) [51] is one of the most commonly used approaches, it is an inversion method based on obtaining cell traction from the deformation of its environment. In these experiments cells are usually cultured on a polyacrylamide gel substrate with known mechanical properties, such that the tractions exerted by cells are then retrieved by solving an inverse elasticity problem for the measured displacements of the substrate [52]. Meanwhile, we can find simialr

techniques choose to culture cells on special environments (e.g. micropillar arrays [53], micromachined substrates [54]) with more explicit mechanical characteristics. However, when it comes to monitoring the interiors of cell masses or *in-vivo* tissues, which they are usually protected by a requisite layer such as a vitelline membrane, these sort of experimental techniques tend to be very limited. Besides, they provide force information limited to specific locations and times. One could theoretically construct detailed spatial and temporal force maps by collating data from multiple specimens, but animal-to-animal variations make such approaches impractical.

Computational models also provided a great deal of information about cell- and tissue-level forces. These models have been typically used in a forward manner, where a user specifies the forces at work in a particular aggregate of cells or other system under study and uses the model to predict the resulting cell shapes and motions. The time-consuming challenge of this approach is figuring out the forces needed to produce a particular morphological outcome. Another possibility is to consider an inverse mechanical problem to infer mechanical forces from geometrical observation, this approch has been applied for computing the contractile forces that coordinate ventral furrow invagination in Drosophila [55] [56] [57]. Different groups have different names for such technique, Video Force Micrscopy (VFM) [57] , Cinemechanometry (CMM) [58], CellFIT [59] [60]. Although, all these methods are based on inverting the equations of mechanical equilibrium, the modeling approaches are fundamentally different, therefore, we can find a considerable variation in the assumptions made about mechanical state of tissue, the parameterization of forces as well as the way imaging data is utilized. Ultimately, the fact that these type of techniques uses dataset of observed deformations as its primary input and from it directly calculates the forces that must act to drive those motions, give the potential to become a standard tool for biologists studying forces within tissues.

1.5 Scope and Outlines

The main objective of this work is to study the possibility of inverting the mechanical equilibrium of Hybrid vertex model [42] in order to infer the set of active forces/contractions form an observed deformation. The aim is to complement experiments with a tool that can propose the spatial and temporal maps of forces from time-lapse images. To achieve this, the following tasks are proposed:

- Writing the inverse mechanical problem of hybrid vertex model and characterizing its solvability.
- Implementing the model in computational platform with post-processing tool, and testing the compatibility between the inverse and direct mechanical problems.
- Extracting kinematic data for microscopic images.
- Applying the proposed methodology to deduce the contractions that drives wound healing.

The present thesis is organized as following: In Chapter 2, we introduce the mathematical formulation of Hybrid vertex models, stating both the *direct* and *inverse* problems, with different forms of regularizations. Then, we present the way how we accessed our methodology based on numerical experiments. Chapter 3 presents an extension of our analysis by repeating the same steps in Chapter 2, while considering the case of a purely vertex model. Chapter 4 is dedicated to the phenomena of wound healing. it presents the modifications that had to be introduced to describe wound healing, along with the result obtained after applying our approach on wound healing of embryonic tissue.

Chapter 2

Inverse Analysis of Hybrid Cell-centered/Vertex Model

In the following chapter, the mathematical formulation of Hybrid Cell-centered/Vertex model is presented, while stating both the *Direct* and *Inverse* mechanical problems. The reader is encouraged to review [61] for more details. Next, we describe how the inverse problem was assessed with the results obtained from numerical experiments.

2.1 Model Topology

In this model, the spatial description of epithelial monolayer is defined by cell-centers *nodes* $\boldsymbol{x} = \{\boldsymbol{x}^1, \ldots, \boldsymbol{x}^{N_{nodes}}\}$, and coupling between two neighboring cells i and j is defined by the presence of a one-dimensional bar element connecting their centers $\boldsymbol{x}^i$ and $\boldsymbol{x}^j$, leading up to a discretization of the tissue into set of triangles $\mathcal{T}^I$ with $I = 1, \ldots, N_{tri}$ as shown by the continuous lines in Figure 2.1. Assuming no extracellular space between cells, the boundary of the cells is defined by a set of connected *vertices* $\boldsymbol{y} = \{\boldsymbol{y}^1, \ldots, \boldsymbol{y}^{N_{tri}}\}$, such that each two neighboring vertices $\boldsymbol{y}^I$ and $\boldsymbol{y}^J$ are connected through one-dimensional bar element which are presented by the dashed lines in Figure 2.1. The position of vertex $\boldsymbol{y}^I$ is defined by barycentric/areal coordinates with respect to triangle $\mathcal{T}^I$, and the relation between nodal positions and vertices is given as

$$\mathbf{y}^I = \sum_{i \in \mathcal{T}^I} N^i(\boldsymbol{\xi}^I)\mathbf{x}^i \tag{2.1}$$

where the summation in eq.(2.1) extends to the three nodes of triangle $\mathcal{T}^I$, and $N^i(\boldsymbol{\xi}^I)$ is the linear shape function of node i evaluated at $\boldsymbol{\xi}^I = \{\xi^I, \eta^I\}$, such that,

$$N^1(\boldsymbol{\xi}^I) = \xi^I \qquad N^2(\boldsymbol{\xi}^I) = \eta^I \qquad N^3(\boldsymbol{\xi}^I) = 1 - \xi^I - \eta^I \tag{2.2}$$

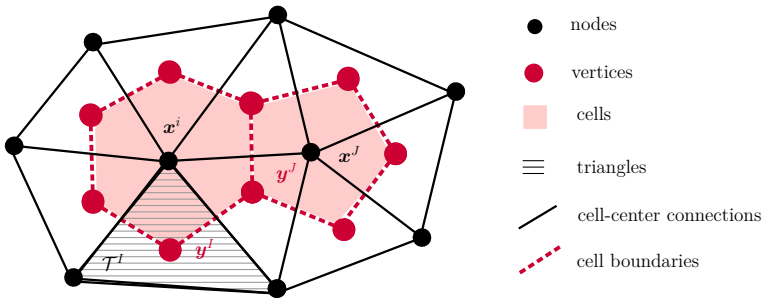

Figure 2.1: Discretisation of tissue into cell-centres (nodes, $\boldsymbol{x}^i$) and cells boundaries (vertices, $\boldsymbol{y}^I$). Nodal network and vertex network are outlined with continuous and dashed lines, respectively.

Practically, the connectivity between nodes is defined using Delaunay triangulation (DT) of nodes $\boldsymbol{x} = \{\boldsymbol{x}^1, \ldots, \boldsymbol{x}^{N_{nodes}}\}$ [62], which basically means that for a given set of nodes one can obtain a complete geometrical description of the tissue, since vertex postions $\boldsymbol{y}$ are defind in terms of nodal positions $\boldsymbol{x}$. Additional procedure might be necessary, such as filtering the skinny triangles that usually appear on the boundary, or adding an off-set of boundary nodes in order to tessellate cells which are in the edges, more details can be found in [42] [61].

2.2 Rheological Model

Each pair of connected nodes ij or vertices IJ are joined with a one-dimensional bar element, for simplicity, we will consider an elastic model (spring) to describe their mechanical behavior, with quadratic strain function

Node-Node elements

$$W_D^{ij}(\boldsymbol{x}) = \frac{1}{2} k_D (\varepsilon_e^{ij})^2 L_0^{ij} \qquad W_D(\boldsymbol{x}) = \sum_{ij=1}^{N_D} W_D^{ij}(\boldsymbol{x}) \tag{2.3}$$

with

$$\varepsilon_e^{ij} = \frac{l^{ij} - L_0^{ij}}{L_0^{ij}} \quad l^{ij} = ||\boldsymbol{x}^i - \boldsymbol{x}^j|| \quad L_0^{ij} = ||\boldsymbol{x}_0^i - \boldsymbol{x}_0^j||$$

In the above expression W_D^{ij} is the *elastic potential* energy of the bar joining node i and j, W_D is the *total energy* of the nodal network, k_D is the material intercellular stiffness, ε_e^{ij} is the elastic strain measure with L_0^{ij}, l^{ij} indicating the current and reference lengths, respectively.

Vertex-Vertex elements

$$W_V^{IJ}(\boldsymbol{y}) = \frac{1}{2} k_V (\varepsilon^{IJ})^2 L_0^{IJ} \qquad W_V(\boldsymbol{y}) = \sum_{IJ=1}^{N_V} W_V^{IJ}(\boldsymbol{y}) \tag{2.4}$$

with

$$\varepsilon^{IJ} = \varepsilon_e^{IJ} + \varepsilon_c^{IJ} \quad \varepsilon_e^{IJ} = \frac{l^{IJ} - L_0^{IJ}}{L_0^{IJ}} \quad l^{IJ} = ||\boldsymbol{y}^I - \boldsymbol{y}^J|| \quad L_0^{IJ} = ||\boldsymbol{y}_0^I - \boldsymbol{y}_0^J||$$

For elements joining vertex I and J, we introduce an additional parameter ε_c^{IJ} presenting the contractility of cell boundaries. For compact formulation contractility is inserted into the strain function, thus, W_V^{IJ} can be interpenetrated as the sum of the *elastic potential* energy of the bar IJ and the active energy due to active cellular force. And the rest of the notation is the same as eq. 2.3, while replacing nodal indices i, j with vertex I, J.

We remark that the above strain function is quadratic with respect to the strain while our strain measure depends nonlinearly on the position $\boldsymbol{x}^i, \boldsymbol{y}^I$. This make the force to vary nonlinearly when the bars turn and the displacements are large, which is the general case considered here. This geometrical nonlinearity can be complemented with material nonlineartiy, considering viscous effects, e.g. [21] [42]. Regardless of the chosen strain function the present work is still applicable and easily extendable as long as the resultant tractions (section 2.4) depend linearly on the contractility ε_c^{IJ} .

2.3 Area Constraint

Cell volume invariance under tissue extension is relevant when the size and the number of cells within the tissue is considered as constant. A two-dimensional area constraint will be imposed here by adding the energy term

$$W_A = \frac{\lambda_A}{2} \sum_{m=1}^{N_{cell}} (A^m - A_0^m)^2 \tag{2.5}$$

where λ_A is a penalisation coefficient and A_0^m and A^m are the initial and the current areas of cell m, respectively.

The area m can be expressed in terms of its vertices by using Gasuss theorem

$$A^m = \int_{\Omega^m} dA = \frac{1}{2} \int_{\partial\Omega^m} \boldsymbol{y}.\boldsymbol{n} ds \tag{2.6}$$

where $\boldsymbol{y}$ is an arbitrary point on the boundary of cell m, ds is the differential segment of the cell boundary and $\boldsymbol{n}$ is the outward normal. Since each cell boundary forms a polygon, we will break the integral over the whole cell boundary into N_m line integrals.

Points between vertices I and J can be obtained by using a linear interpolation

$$\boldsymbol{y} = q^I(\alpha)\boldsymbol{y}^I + q^J(\alpha)\boldsymbol{y}^J \tag{2.7}$$

with $\alpha \in [-1, 1]$ a local coordinate along the cell boundary segment IJ, and $q^I(\alpha) = \frac{1}{2}(1-\alpha)$ and $q^J(\alpha) = \frac{1}{2}(1+\alpha)$ the interpolation functions. By inserting eq.(2.7) into eq.(2.6) and noting that $ds = l^{IJ}\frac{d\alpha}{2}$, with $l^{IJ} = ||\boldsymbol{y}^I - \boldsymbol{y}^J||$, we have

$$A^m = \frac{1}{2}\sum_{IJ\in P^m}^{N_m}\int_{-1}^{1}\sum_{I} q^I(\alpha)\boldsymbol{y}^I.\boldsymbol{n}^{IJ}\frac{l^{IJ}}{2}d\alpha = \frac{1}{2}\sum_{IJ\in P^m}^{N_m}\frac{l^{IJ}}{2}(\boldsymbol{y}^I + \boldsymbol{y}^J).\boldsymbol{n}^{IJ} \tag{2.8}$$

where P^m denote the segments of the polygon that surround node $\boldsymbol{x}^m$ (see Figure 2.1). The expression above can be simplified as

$$A^m = \frac{1}{2}\sum_{IJ\in P^m}^{N_m}(\boldsymbol{y}^I \times \boldsymbol{y}^J).\boldsymbol{e}_z = \frac{1}{2}\sum_{IJ\in P^m}^{N_m}\boldsymbol{y}^I.\mathbf{J}\boldsymbol{y}^J \tag{2.9}$$

where matrix $\mathbf{J} = \begin{bmatrix} 0 & -1 \\ 1 & 0 \end{bmatrix}$ is such that $(\boldsymbol{y}^I \times \boldsymbol{y}^J).\boldsymbol{e}_z = \boldsymbol{y}^I.\mathbf{J}\boldsymbol{y}^J$. Finally the total area of the whole set on N_{cells} in the tissue A_T, can be expressed as

$$A_T = \frac{1}{2}\sum_{m=1}^{N_{cells}}\sum_{IJ\in P^m}\boldsymbol{y}^I.\mathbf{J}\boldsymbol{y}^J \tag{2.10}$$

2.4 Mechanical Equilibrium

The mechanical equilibrium of the bar elements of the two network is obtained by minimizing the total energy $W_D(\boldsymbol{x}) + W_V(\boldsymbol{y}(\boldsymbol{x})) + W_A(\boldsymbol{y}(\boldsymbol{x}))$ considering the principal kinematic variable $\boldsymbol{x}$

$$\boldsymbol{x}^* = \text{argmin}_x(W_D(\boldsymbol{x}) + W_V(\boldsymbol{y}(\boldsymbol{x})) + W_A(\boldsymbol{y}(\boldsymbol{x}))) \tag{2.11}$$

$$\frac{\partial W_D(\boldsymbol{x})}{\partial \boldsymbol{x}^i} + \frac{\partial W_V(\boldsymbol{y}(\boldsymbol{x}))}{\partial \boldsymbol{x}^i} + \frac{\partial W_A(\boldsymbol{y}(\boldsymbol{x}))}{\partial \boldsymbol{x}^i} = \mathbf{0}, \quad i = 1, \ldots, N_{nodes} \tag{2.12}$$

which also can be interpreted as the nodal force equilibrium summing the contributions coming from nodal network $\mathbf{g}_D^i$, vertex network $\mathbf{g}_V^i$ and area constraint $\mathbf{g}_A^i$

$$\mathbf{g}_x^i := \mathbf{g}_D^i + \mathbf{g}_V^i + \mathbf{g}_A^i = \mathbf{0}, \quad i = 1, \ldots, N_{nodes} \tag{2.13}$$

such that $\mathbf{g}_D^i$ is summation of tractions at node i due to the bars connecting node i with neighboring nodes S^i

$$\mathbf{g}_D^i := \sum_{j\in S^i}\frac{\partial W_D^{ij}}{\partial \boldsymbol{x}^i} \tag{2.14}$$

while $\mathbf{g}_V^i$ is the contributions coming from the set of vertices acting on node i through the kinematic constrain defined in eq.(2.1)

$$\mathbf{g}_V^i := \frac{\partial W_V}{\partial \boldsymbol{x}^i} = \sum_{IJ} \left(\frac{\partial W_V^{IJ}}{\partial \boldsymbol{y}^I} \frac{\partial \boldsymbol{y}^I}{\partial \boldsymbol{x}^i} + \frac{\partial W_V^{IJ}}{\partial \boldsymbol{y}^J} \frac{\partial \boldsymbol{y}^J}{\partial \boldsymbol{x}^i} \right) = \sum_{I \in B^i} N^i(\boldsymbol{\xi}^I) \sum_{J \in S^I} \frac{\partial W_V^{IJ}}{\partial \boldsymbol{y}^I} \tag{2.15}$$

with B^i is the set of vertices on the boundary of cell i, centered on $\boldsymbol{x}^i$, and S^I is the set of vertices connected to vertex I.

From the expression of W_D^{ij} and W_V^{ij} in eq.(2.3) and (2.4) we can define the tractions in the bar elements between nodes ij and vertices IJ as following

$$\mathbf{t}_D^{ij} = -\mathbf{t}_D^{ji} = \frac{\partial W_D^{ij}}{\partial \boldsymbol{x}^i} = k_D \, \varepsilon_e^{ij} \, \mathbf{e}^{ij} \qquad \mathbf{t}_V^{IJ} = -\mathbf{t}_V^{JI} = \frac{\partial W_V^{IJ}}{\partial \boldsymbol{y}^I} = k_V \, \varepsilon^{IJ} \, \mathbf{e}^{IJ} \tag{2.16}$$

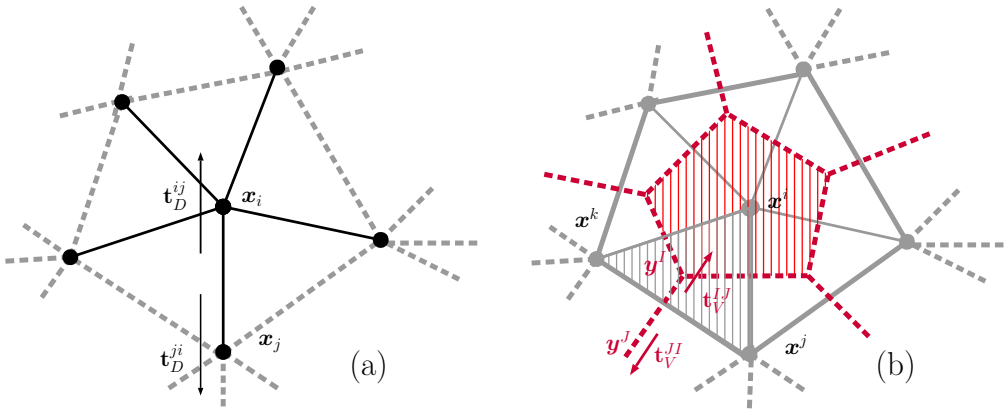

Figure 2.2: (a) Schematic view of node i connectivity (continuous lines), within the rest of the network (dashed lines) and traction vector $\mathbf{t}_D^{ij}$. (b) Cell boundary (dashed polygon) corresponding to node i. Barycentric tessellation of triangle ijk results to triple-junction $\boldsymbol{y}^I$. Vector $\mathbf{t}_V^{IJ}$ represents the traction between vertices $\boldsymbol{y}^I$ and $\boldsymbol{y}^J$ along the shared boundary of cells $\boldsymbol{x}^j$ and $\boldsymbol{x}^k$.

And the nodal contribution arising from the area constraint takes that following from

$$\mathbf{g}_A^i := \frac{\partial W_A}{\partial \boldsymbol{x}^i} = \frac{\lambda_A}{2} \mathbf{J} \sum_{m \in \bar{S}^i} (A^m - A_0^m) \sum_{IJ \in P^m} (N^i(\boldsymbol{\xi}^I) \boldsymbol{y}^J - N^i(\boldsymbol{\xi}^J) \boldsymbol{y}^I) \tag{2.17}$$

where the set $\bar{S}^i$ in the first summation includes the nodes that surround node $\boldsymbol{x}^i$ and also node $\boldsymbol{x}^i$ itself.

The total mechanical equilibrium of the system can be expressed by the set of nonlinear equations

$$\mathbf{g}_x(\boldsymbol{x}, \boldsymbol{\varepsilon}_c) = \mathbf{0} \tag{2.18}$$

with

$$\begin{aligned}\mathbf{g}_x^i = &\sum_{j\in\mathcal{S}^i} \mathbf{t}_D^{ij} + \sum_{I\in B^i} N^i(\boldsymbol{\xi}^I) \sum_{J\in\mathcal{S}^I} \mathbf{t}_V^{IJ} \qquad i = 1, \ldots, N_{nodes} \\ &+ \frac{\lambda_A}{2}\mathbf{J} \sum_{m\in\bar{S}^i} (A^m - A_0^m) \sum_{IJ\in P^m} (N^i(\boldsymbol{\xi}^I)\boldsymbol{y}^J - N^i(\boldsymbol{\xi}^J)\boldsymbol{y}^I) = \mathbf{0}\end{aligned}$$

2.5 Direct Problem

For a given set of contractions $\boldsymbol{\varepsilon}_c = \{\varepsilon_c^1, \varepsilon_c^2, ..., \varepsilon_c^{N_V}\}$ obtain the set of nodal positions $\boldsymbol{x} = \{\boldsymbol{x}^1, \ldots, \boldsymbol{x}^{N_{nodes}}\}$ that satisfy the mechanical equilibrium,

$$\mathbf{g}_x(\boldsymbol{x}) = \mathbf{0} \tag{2.19}$$

which also can be seen as solving the above nonlinear equations. Newton's method can be cast as

$$\Delta\boldsymbol{x}^{k+1} = -(\mathbf{K}_{xx}(\boldsymbol{x}^k))^{-1}\, \mathbf{g}_x(\boldsymbol{x}^k) \tag{2.20}$$

where $\mathbf{K}_{xx} \in \mathbb{R}^{2N_{nodes}\times 2N_{nodes}}$ is the Jacobian matrix with enters of the following partial derivatives

$$\mathbf{K}_{xx}^{ij} = \frac{\partial \mathbf{g}_x^i}{\partial \boldsymbol{x}^j} = \frac{\partial \mathbf{g}_D^i}{\partial \boldsymbol{x}^j} + \frac{\partial \mathbf{g}_V^i}{\partial \boldsymbol{x}^j} + \frac{\partial \mathbf{g}_A^i}{\partial \boldsymbol{x}^j} \tag{2.21}$$

with

$$\frac{\partial \mathbf{g}_D^i}{\partial \boldsymbol{x}^j} = \sum_{j\in\mathcal{S}^i} \mathbf{K}_t^{ij} \qquad \frac{\partial \mathbf{g}_V^i}{\partial \boldsymbol{x}^j} = \sum_{I\in B^i} N^i(\xi^I) \sum_{J\in\mathcal{S}^I} \mathbf{K}_t^{IJ}(N^j(\boldsymbol{\xi}^J) - N^j(\boldsymbol{\xi}^I))$$

$$\begin{aligned}\frac{\partial \mathbf{g}_A^i}{\partial \boldsymbol{x}^j} = &\frac{\lambda_A}{2}\mathbf{J} \sum_{m=\bar{S}^i} (A^m - A_0^m) \sum_{IJ\in P^m} (N^i(\boldsymbol{\xi}^I)N^j(\boldsymbol{\xi}^J) - N^i(\boldsymbol{\xi}^J)N^j(\boldsymbol{\xi}^I)) \\ &+ \frac{\lambda_A}{4} \sum_{m=\bar{S}^i} \sum_{IJ\in P^m} \mathbf{J}\big(N^i(\boldsymbol{\xi}^I)\boldsymbol{y}^J - N^i(\boldsymbol{\xi}^J)\boldsymbol{y}^I\big) \otimes \sum_{KL\in P^m} \mathbf{J}\big(N^j(\boldsymbol{\xi}^K)\boldsymbol{y}^L - N^j(\boldsymbol{\xi}^L)\boldsymbol{y}^K\big),\end{aligned}$$

In the above expression $\mathbf{K}_t^{IJ}$ denote the derivative of the traction vector defined in eq.(2.16) such that

$$\mathbf{K}_t^{IJ} := \frac{\partial \mathbf{t}_V^{IJ}}{\partial \boldsymbol{y}^J} = -\frac{\partial \mathbf{t}_V^{JI}}{\partial \boldsymbol{y}^J} = -\mathbf{K}_t^{JJ} = -\mathbf{K}_t^{II} = \mathbf{K}_t^{JI} \tag{2.22}$$

and

$$\mathbf{K}_t^{IJ} = -\frac{k_V}{l^{IJ}}\,\mathbf{I} + \frac{k_V(\varepsilon_c^{IJ} - 1)}{l^{IJ}}\,(\boldsymbol{e}^{IJ} \otimes \boldsymbol{e}^{IJ}) \tag{2.23}$$

Similar expressions can be obtained for $\mathbf{K}_t^{ij} = \frac{\partial \mathbf{t}_D^{ij}}{\partial \boldsymbol{x}^j}$ by replacing the IJ with ij.

2.6 Inverse Problem

For a given set of nodal position $\boldsymbol{x} = \{\boldsymbol{x}^i, \ldots, \boldsymbol{x}^{N_{nodes}}\}$ obtain the contractility $\boldsymbol{\varepsilon}_c = \{\varepsilon_c^1, \varepsilon_c^2, ..., \varepsilon_c^{N_V}\}$ that satisfy the mechanical equilibrium defined in eq.(2.18). First, lets write the problem in a least-squares fashion,

$$\min_{\boldsymbol{\varepsilon_c}} \frac{1}{2}||\mathbf{g}_x(\boldsymbol{\varepsilon}_c)||_2^2 \tag{2.24}$$

Since the residual vector $\mathbf{g}_x$ depends linearly on the contractions $\boldsymbol{\varepsilon}_c$, it can be decoupled such that

$$\min_{\boldsymbol{\varepsilon_c}} \frac{1}{2}||\mathbf{K}_{x\varepsilon}\boldsymbol{\varepsilon}_c + \mathbf{q}_x||_2^2 \tag{2.25}$$

where $\mathbf{K}_{x\varepsilon} \in \mathbb{R}^{2N_{nodes} \times N_V}$ is a non-squared matrix that can be seen as the Jacobian matrix of the partial derivatives $(\mathbf{K}_{x\varepsilon})_{il} = \partial \mathbf{g}_x^i / \partial \varepsilon_c^l$ and $\mathbf{q}_x \in \mathbb{R}^{2N_{nodes}}$ is the residual vector due to the elastic potential and area constraint,

$$\mathbf{K}_{x\varepsilon}^{il} = \sum_{I \in B^i \in E^l} N^i(\boldsymbol{\xi}^I) \sum_{J \in \mathcal{S}^I \in E^l} k_V \boldsymbol{e}^{IJ} \tag{2.26}$$

$$\mathbf{q}_x^i = \mathbf{g}_D^i + \sum_{I \in B^i} N^i(\boldsymbol{\xi}^I) \sum_{J \in \mathcal{S}^I} k_V \varepsilon_e^{IJ} \boldsymbol{e}^{IJ} + \mathbf{g}_A^i \tag{2.27}$$

where E^l is the two vertices connecting bar l.

One may notice that the well-posedness of the least-squares problem defined in eq.(2.25) is highly dependent on the size of $\mathbf{K}_{x\varepsilon}$ and $\mathbf{q}_x$ or more specifically the number of contractile bars (unknowns) N_V and degrees-of-freedom $2N_{nodes}$. Figure 2.3 shows these numbers for a rectangular tissue with different sizes, it can be seen for most of the cases $N_V > 2N_{nodes}$ which makes $\mathbf{K}_{x\varepsilon}$ non-squared matrix with more column then rows.

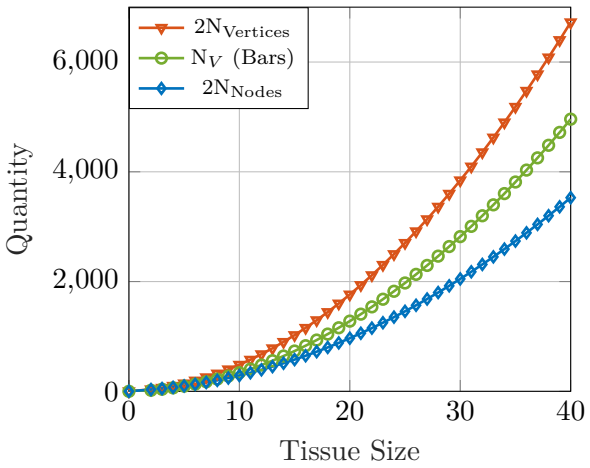

Figure 2.3: The size of variables $\boldsymbol{x}, \boldsymbol{y}, \boldsymbol{\varepsilon}_c$ with different tissue size.

Therefore, the solution of the least-squares problem defined in eq.(2.25) with an L_2-norm fidelity constraint can not be unique, this can be demonstrated by checking the kernel of the resultant linear mapping when we minimize with respect to $\boldsymbol{\varepsilon}_c$

$$\mathbf{K}_{x\varepsilon}^T \mathbf{K}_{x\varepsilon} \boldsymbol{\varepsilon}_c = -\mathbf{K}_{x\varepsilon}^T \mathbf{q}_x \tag{2.28}$$

with $\big(\mathbf{K}_{x\varepsilon}^T \mathbf{K}_{x\varepsilon}\big) \in \mathbb{R}^{N_V \times N_V}$ and $\big(\mathbf{K}_{x\varepsilon}^T \mathbf{q}_x\big) \in \mathbb{R}^{N_V}$.

It can be stated that when $N_V > 2N_{nodes}$ the above system of equation has no solution or infinite number of solutions, based on the fact that

$$\dim\big(\mathrm{im}(\mathbf{K}_{x\varepsilon}^T \mathbf{K}_{x\varepsilon})\big) \leq min\Big(\dim\big(\mathrm{im}(\mathbf{K}_{x\varepsilon}^T)\big), \dim\big(\mathrm{im}(\mathbf{K}_{x\varepsilon})\big)\Big) \leq 2N_{nodes} \tag{2.29}$$

and since

$$\dim\big(\mathrm{im}(\mathbf{K}_{x\varepsilon}^T \mathbf{K}_{x\varepsilon})\big) + \dim\big(\ker(\mathbf{K}_{x\varepsilon}^T \mathbf{K}_{x\varepsilon})\big) = N_V \tag{2.30}$$

it implies that

$$\dim\big(\ker(\mathbf{K}_{x\varepsilon}^T \mathbf{K}_{x\varepsilon})\big) \geq N_V - 2N_{nodes} > 0 \tag{2.31}$$

which basically indicate that the kernel of the linear mapping in eq.(2.28) is full as long as $N_V > 2N_{nodes}$ with the matrix $\mathbf{K}_{x\varepsilon}^T \mathbf{K}_{x\varepsilon}$ being singular. In following sections we present different attempts to regularize the inverse problem, while imposing additional criteria on our solution.

2.6.1 Tikhonov regularization (TR)

First, we have considered the most common from of regularization, by penalizing large $||\boldsymbol{\varepsilon}_c||$, such that

$$\min_{\boldsymbol{\varepsilon}_c} \quad ||\mathbf{K}_{x\varepsilon} \boldsymbol{\varepsilon}_c + \mathbf{q}_x||_2^2 + \delta ||\boldsymbol{\varepsilon}_c||_2^2 \tag{2.32}$$

with $\delta > 0$, adding the extra penalty term introduces the hypotheses that $\boldsymbol{\varepsilon}_c$ is not too large. Based on the value of δ the above bi-criterion minimization compromise between minimizing the main objective ($||\mathbf{K}_{x\varepsilon} \boldsymbol{\varepsilon}_c + \mathbf{q}_x||_2^2$) and keeping $||\boldsymbol{\varepsilon}_c||_2^2$ of reasonable size. And the the analytical solution can be written as

$$\big(\mathbf{K}_{x\varepsilon}^T \mathbf{K}_{x\varepsilon} + \delta \mathbf{I}\big) \boldsymbol{\varepsilon}_c = -\mathbf{K}_{x\varepsilon}^T \mathbf{q}_x \tag{2.33}$$

with $\mathbf{I}$ being the identity matrix.

2.6.2 Least L_2-norm

Another option was to consider a least-norm problem while taking the mechanical equilibrium of the system as constraint,

$$\begin{aligned} \min_{\boldsymbol{\varepsilon}_c} \quad & \frac{1}{2}||\boldsymbol{\varepsilon}_c||_2^2 \\ \text{subject to} \quad & \mathbf{K}_{x\varepsilon}\boldsymbol{\varepsilon}_c = -\mathbf{q}_x \end{aligned} \tag{2.34}$$

The above constrained minimization can be interpreted as choosing out of all possible solutions the set of $\boldsymbol{\varepsilon}_c$ with minimum L_2-norm. The corresponding Lagrangian of the problem can be written as

$$L(\boldsymbol{\varepsilon}_c, \nu) = \frac{1}{2}\boldsymbol{\varepsilon}_c^T\boldsymbol{\varepsilon}_c + \nu^T\big(\mathbf{K}_{x\varepsilon}\boldsymbol{\varepsilon}_c + \mathbf{q}_x\big) \tag{2.35}$$

with ν being the vector of Lagrange multipliers, minimizing with respect $\boldsymbol{\varepsilon}_c$ and ν gives

$$\nabla_{\boldsymbol{\varepsilon}_c} L = \boldsymbol{\varepsilon}_{\boldsymbol{c}} + \mathbf{K}_{x\varepsilon}^T\nu = \mathbf{0} \tag{2.36}$$

$$\nabla_{\nu} L = \mathbf{K}_{x\varepsilon}\boldsymbol{\varepsilon}_c + \mathbf{q}_x = \mathbf{0} \tag{2.37}$$

multiplying the first eq.(2.36) by $\mathbf{K}_{x\varepsilon}$ and then substituting by the second eq.(2.37) leads to

$$\mathbf{K}_{x\varepsilon}\mathbf{K}_{x\varepsilon}^T\nu = \mathbf{q}_x \tag{2.38}$$

thus, the solution is obtained by solving the above linear system for the Lagrange multipliers and then substituting back in eq.(2.36), which also can be written as

$$\boldsymbol{\varepsilon}_c = \mathbf{K}_{x\varepsilon}^{\dagger}\mathbf{q}_x = -\mathbf{K}_{x\varepsilon}^T(\mathbf{K}_{x\varepsilon}\mathbf{K}_{x\varepsilon}^T)^{-1}\mathbf{q}_x \tag{2.39}$$

with $\mathbf{K}_{x\varepsilon}^{\dagger}$ is *MoorePenrose left* pseudoinverse of matrix $\mathbf{K}_{x\varepsilon}$.

2.6.3 Least L_∞-norm

Here we consider another constrained minimization problem, but instead, out of all possible solution our objective is to obtain the set of contractions $\boldsymbol{\varepsilon}_c$ with minimum L_∞ norm.

$$\begin{aligned} \min_{\boldsymbol{\varepsilon}_c} \quad & ||\boldsymbol{\varepsilon}_c||_\infty \\ \text{subject to} \quad & \mathbf{K}_{x\varepsilon}\boldsymbol{\varepsilon}_c = -\mathbf{q}_x \end{aligned} \tag{2.40}$$

The above problem might be rewritten in linear programming formalism, eliminating the L_∞-norm by introducing inequality constrained, such as

$$\begin{aligned} \min \quad & z \\ \text{subject to} \quad & -z \leq \boldsymbol{\varepsilon}_c^i \leq z, \quad i = 1, \ldots, N_V, \\ & \mathbf{K}_{x\varepsilon}\boldsymbol{\varepsilon}_c = -\mathbf{q}_x \end{aligned} \tag{2.41}$$

Implementing a solver of the above problem was not broached in this work, instead, the external package *CVX* for solving convex programs was being used [63].

2.6.4 Minimum vertex residual(VR)

In the following problem we are aiming to obtain the set of contractions $\boldsymbol{\varepsilon}_c$ with minimum residual at vertices, such that

$$\begin{aligned} \min_{\boldsymbol{\varepsilon}_c} \quad & \frac{1}{2}||\mathbf{K}_{y\varepsilon}\boldsymbol{\varepsilon}_c + \bar{\mathbf{q}}_y||_2^2 \\ \text{subject to} \quad & \mathbf{K}_{x\varepsilon}\boldsymbol{\varepsilon}_c = -\mathbf{q}_x \end{aligned} \tag{2.42}$$

with

$$\mathbf{K}_{y\varepsilon}^{I,IJ} = k_V e^{IJ} \qquad \bar{\mathbf{q}}_y^I = \sum_{J\in\mathcal{S}^I} k_V \varepsilon_e^{IJ} \boldsymbol{e}^{IJ} \tag{2.43}$$

The objective to be minimized in the above problem, represent the L_2 residual coming from the elastic potential on vertices. It should be remarked that such a criteria is not true, according to the mechanical equilibrium defined in section 2.4. Our definition implies zero residual only on nodes, therefore, it allows vertices (boundary of cells) to be unrelaxed. In problem (2.42) we are seeking for that set of contractiles $\boldsymbol{\varepsilon}_c$ that satisfy the mechanical equilibrium with minimum residual at vertices. The corresponding Lagrangian can be written as

$$L(\boldsymbol{\varepsilon}_c, \nu) = \frac{1}{2}\big(\mathbf{K}_{y\varepsilon}\boldsymbol{\varepsilon}_c + \bar{\mathbf{q}}_y\big)^T\big(\mathbf{K}_{y\varepsilon}\boldsymbol{\varepsilon}_c + \bar{\mathbf{q}}_y\big) + \nu^T\big(\mathbf{K}_{x\varepsilon}\boldsymbol{\varepsilon}_c\boldsymbol{\varepsilon}_c + \mathbf{q}_x\big) \tag{2.44}$$

with ν being the vector of Lagrange multipliers. Now, if we take the gradients $\nabla_{\boldsymbol{\varepsilon}} L$ and $\nabla_\nu L$, the solution can be obtained by solving the following linear system

$$\begin{bmatrix} \mathbf{K}_{y\varepsilon}^T\mathbf{K}_{y\varepsilon} & \mathbf{K}_{x\varepsilon}^T \\ \mathbf{K}_{x\varepsilon} & \mathbf{0} \end{bmatrix} \begin{bmatrix} \varepsilon_c \\ \nu \end{bmatrix} = \begin{bmatrix} -\mathbf{K}_{y\varepsilon}^T\bar{\mathbf{q}}_y \\ \mathbf{q}_x \end{bmatrix} \tag{2.45}$$

2.7 Numerical Experiments

The following section describes the numerical tests performed to assess the regularization of the inverse problem.

The main idea of the inverse problem is to obtain the set of cellular contractions $\boldsymbol{\varepsilon}_c$ form a given set of nodal displacements $\boldsymbol{x}$. This implies considering a initial configuration of nodes in which the model is initiated. Then, as the tissue deforms the only necessity is to keep track of nodal positions, since the connectivity is initially defined and the position of vertices is given by eq.(2.1).

In these numerical test, we try to obtain $\boldsymbol{\varepsilon}_c$ from a deformation which is manufactured by prescribed values of $\boldsymbol{\varepsilon}_c$. In this way we are testing the consistency between the direct and inverse problems. As shown in Figure 2.4, these tests basically involve solving direct problem for a specified set of $\boldsymbol{\varepsilon}_c$, and from the resultant nodal displacement, the values of $\boldsymbol{\varepsilon}_c$ are approximated by solving inverse problem.

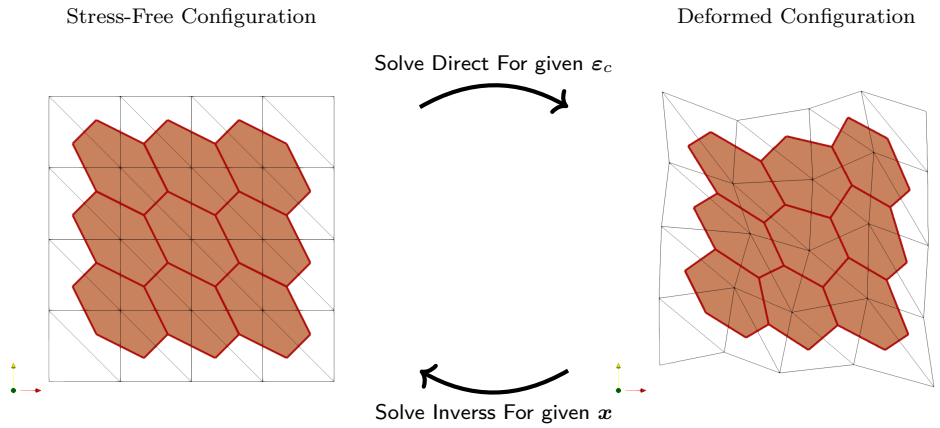

Figure 2.4: Illustration of the numerical experiments, which involves generating a deformed configuration by a specified ε_c (Solving Direct), then, form the deformation the values of ε_c are approximated (Solving Inverse).

2.7.1 Case Study

We have considered two rectangular tissues with two different size 10×10 and 20×20, Figure 2.5. These two sizes were chosen to be large enough to represent the general case of the inverse problem. From Figure 2.5(c), one should expect changes in the nature of the problem in cases with tissues smaller than 10. This is simply because the variation between the number of unknowns N_V and the number of equalities $2N_{nodes}$ is not consistent in those cases,

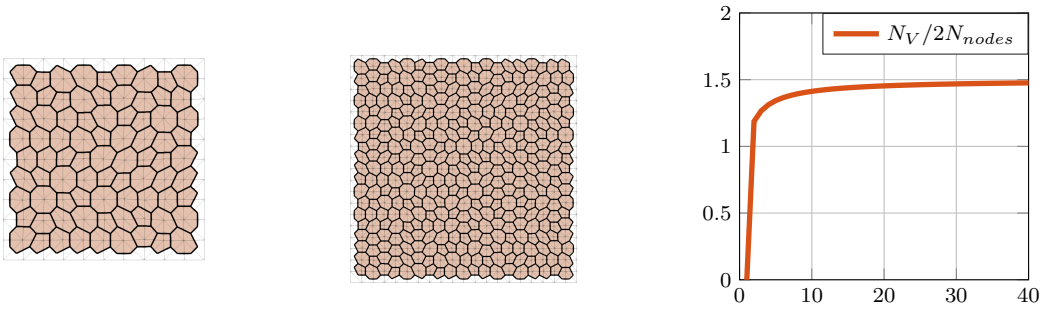

(a) 10×10 (b) 20×20 (c)

Figure 2.5: (a), (b) The initial configuration of 10×10 and 20×20 tissues , with fixed boundary at the left $x = 0$ and right edges $x = 10/x = 20$. (c) The ratio of unknowns (contractile bars N_V) to equalities (Dofs N_{nodes}) with different tissues sizes (x-axes).

The configurations shown in Figure 2.5 are considered as the reference or (stress-free) configurations, which means, the initial lengths L_0 and areas A_0 are computed in these configurations. Also, we are considering fixed boundary on the left and right edges of the tissues, while the upper and lower boundaries are set without constraint.

From the two initial configuration in Figure 2.5 several deformation were generated after choosing various combination of cellular contractions $\boldsymbol{\varepsilon}_c$, see Figure 2.6. To produce these deformations, direct problem was solved using Newton method eq.(2.20), while explicitly fixing the left and right boundary by eliminating the rows and columns corresponding to boundary nodes. These set of deformations along with initial configuration will serve as the main input for the inverse problem.

2.7.2 Error measurement

In Figure 2.7 we shows the relative error of the approximated contractions $\boldsymbol{\varepsilon}_c$ (the one obtained by solving inverse problem) with respect to the exact contractions $\boldsymbol{\varepsilon}_c^{exact}$ (the one used while solving direct problem), considering the following error measurement

$$e_c = \frac{||\boldsymbol{\varepsilon}_c - \boldsymbol{\varepsilon}_c^{exact}||_2}{||\boldsymbol{\varepsilon}_c^{exact}||_2} \tag{2.46}$$

2.7.3 Effect of boundary condition

In the course of these tests, it has been observed that the main factor effecting the accuracy of the inverse solution is how boundaries are treated. In Figure 2.7 we show the values of error while two strategies are considered; the first is to exclude equalities that correspond to nodes which are located in the fix boundary (left and right edges), Figures 4.8(d) and 2.7(b). And the second is to include these nodes along with their associated residual (reactions), Figure 2.7(c) and 2.7(d).

It is true that, the first choice seem to be the most proper way to handle the boundary conditions, due to the lack of information about the behavior or/and nature of the boundary in practice, simply because experimental images usually restricted on an aggregation of cells out of a larger system. And by eliminating boundary nodes the ambiguity of the boundary condition is well present. However, when this criteria was considered, the values of error was high, see Figure 4.8(d) and 2.7(b), and Figure 2.8, 2.9 and 2.10 shows the obtained values of $\boldsymbol{\varepsilon}_c$. Having that high values of error may not be surprising, if we take into account that eliminating boundary nodes dose not only obscure the problem from including the reactions, but also the minimization problem loses more equalities which mean that the set of contractilites $\boldsymbol{\varepsilon}_c$ that satisfy the mechanical equilibrium (optimal value) becomes larger.

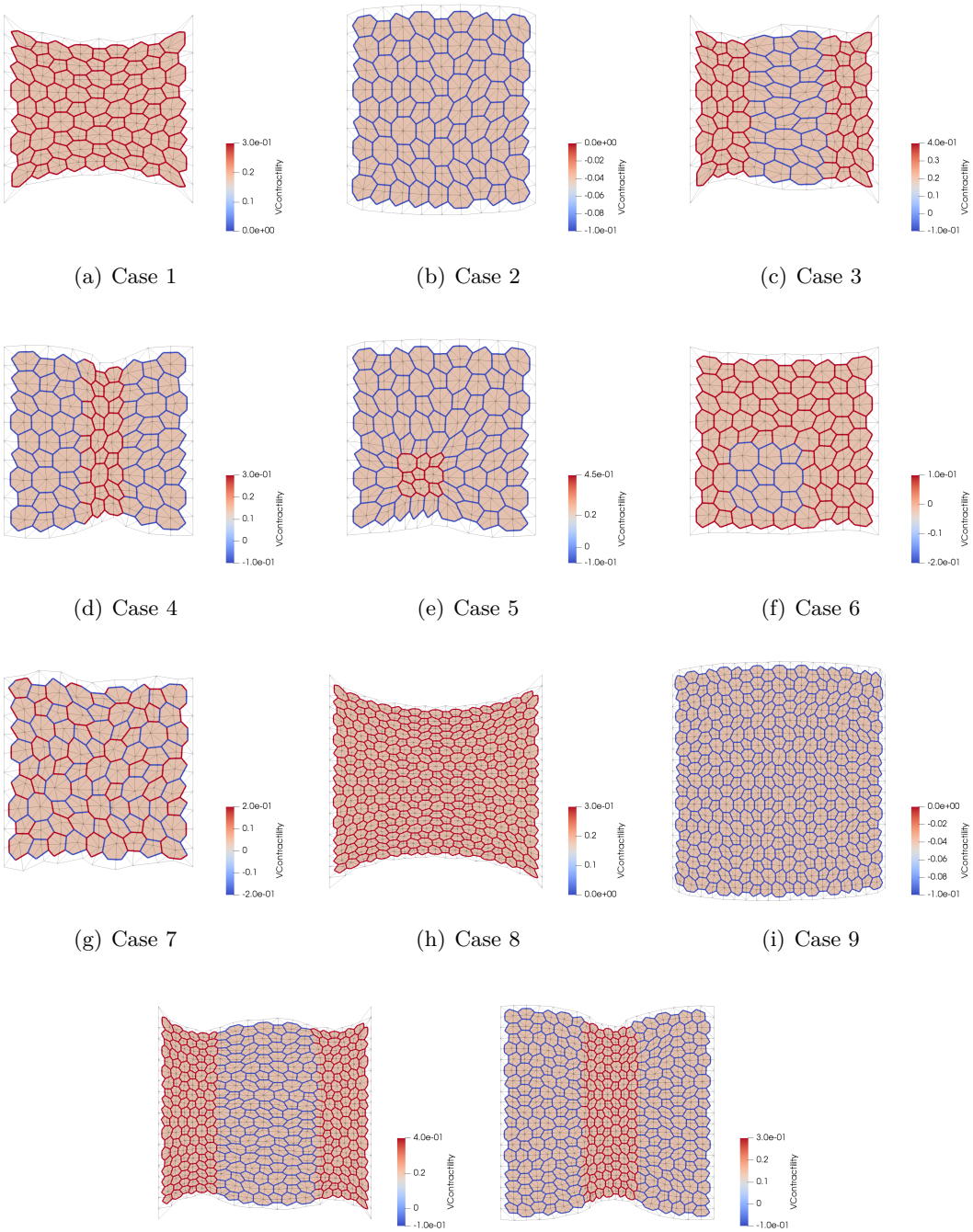

(a) Case 1 (b) Case 2 (c) Case 3

(d) Case 4 (e) Case 5 (f) Case 6

(g) Case 7 (h) Case 8 (i) Case 9

(j) Case 10 (k) Case 11

Figure 2.6: Different deformed tissues used as an input for inverse analysis, the colored contours illustrate the prescribed values of $\boldsymbol{\varepsilon}_c$, while the chosen numerical parameters were $k_D = 0.2$, $k_V = 1$ and $\lambda_A = 10$.

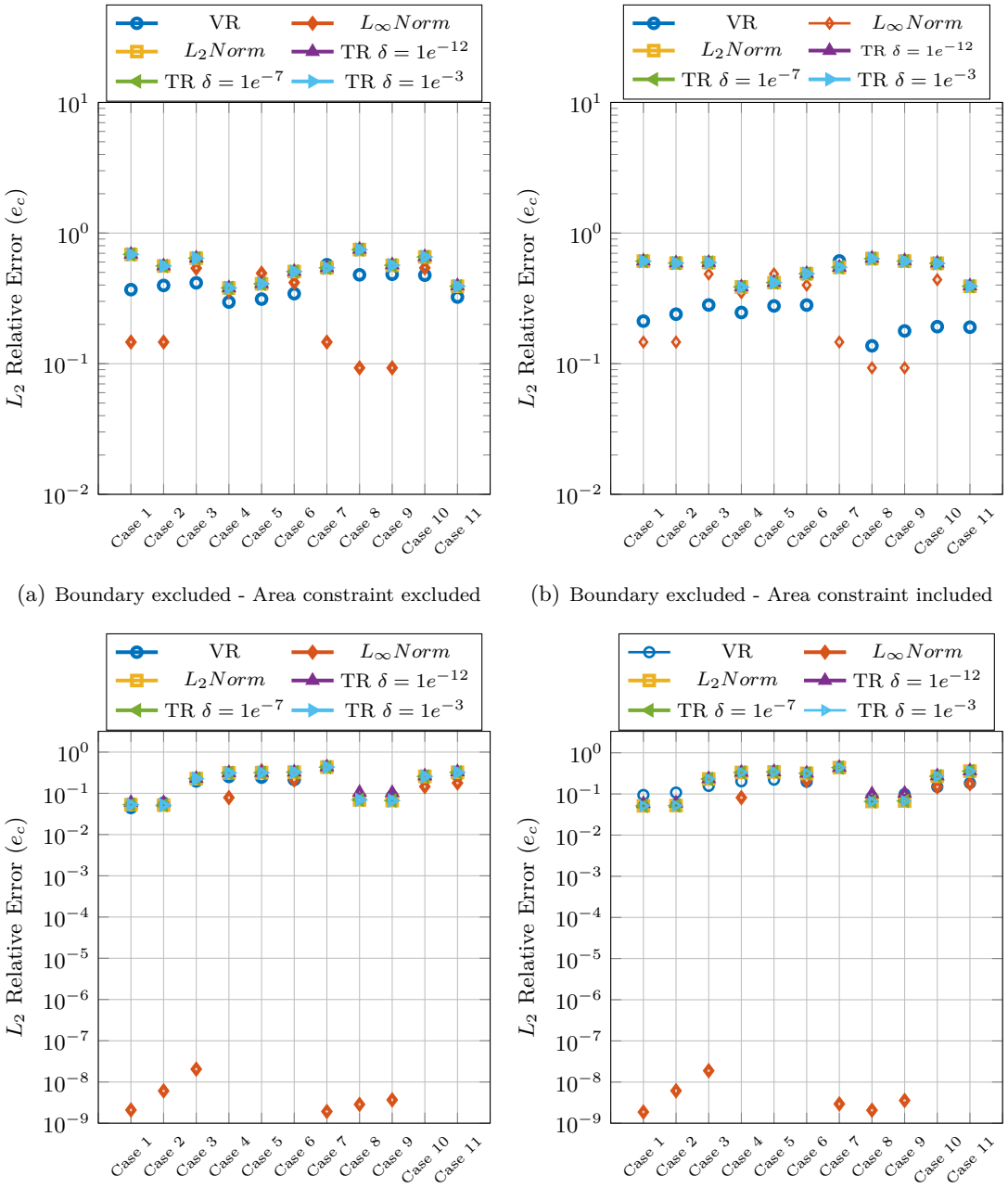

(a) Boundary excluded - Area constraint excluded

(b) Boundary excluded - Area constraint included

(c) Boundary included - Area constraint excluded

(d) Boundary included - Area constraint included

Figure 2.7: Relative error of the obtained contractions ε_c, for the cases in figure 2.6.

Furthermore, improvement can be observed when boundary nodes are included, see Figure 2.7(c) and 2.7(d), especially for cases with more uniform contractions. This observation demonstrate the importance of including what is acting on the boundary of the tissue. However, applying such criteria in practice might be very challenging since the only input will be the deformed configuration, therefore, a proper hypothesis need to be introduced to approximate the residual on the boundary (reactions).

2.7.4 Regularization criteria

As it might be noticed from Figure 2.7, it is unclear if one of the proposed regularization methods is able to serve the general case. For example, using L_∞-norm tend to be the best choice when it comes to cases with more uniform contractions, even when the boundary is excluded, one can notice from Figure 2.9 that the error is limited only to boundary elements, however, in cases with more locally concentrated variation L_∞ norm fails in obtaining adequate values.

Minimizing the residual on vertices (VR), on the other hand tend to be more valid criteria in cases with area constraint, see Figure2.7(b). In such cases this strategy showed more stable results, with relative error not higher then %25 . This suggest that our definition of mechanical equilibrium tend to have more relaxed vertices when the area of the cell is penalized.

Furthermore, using least L_2-norm have given the same results as Tikhonov regularization, while changing the regularization parameter δ did not show any noticeable difference on the values of contractility. It was observed that for most of the cases, when $\delta > 10^{-3}$ the results start to become inconsistent with mechanical equilibrium, and for $\delta < 10^{-12}$ the condition number of the linear system in eq.(2.33) blows up. Regardless, one can notice that both least L_2-norm and the regularized Least-squares have given poor fit, especially when boundary nodes are excluded.

We remark here that all the obtained contractions do satisfy our definition of mechanical equilibrium, in other words, if we solve a direct problem using the obtained values, we retrieve the same deformation (as shown in Figures 2.8 2.9 2.10). For, cases where the uniqueness of the solution is not the main interest using least L_2-norm is the most convenient way since it involves solving a linear system for the Lagrange Multipliers only (eq.(2.38)) with size of $2N_{nodes}$.

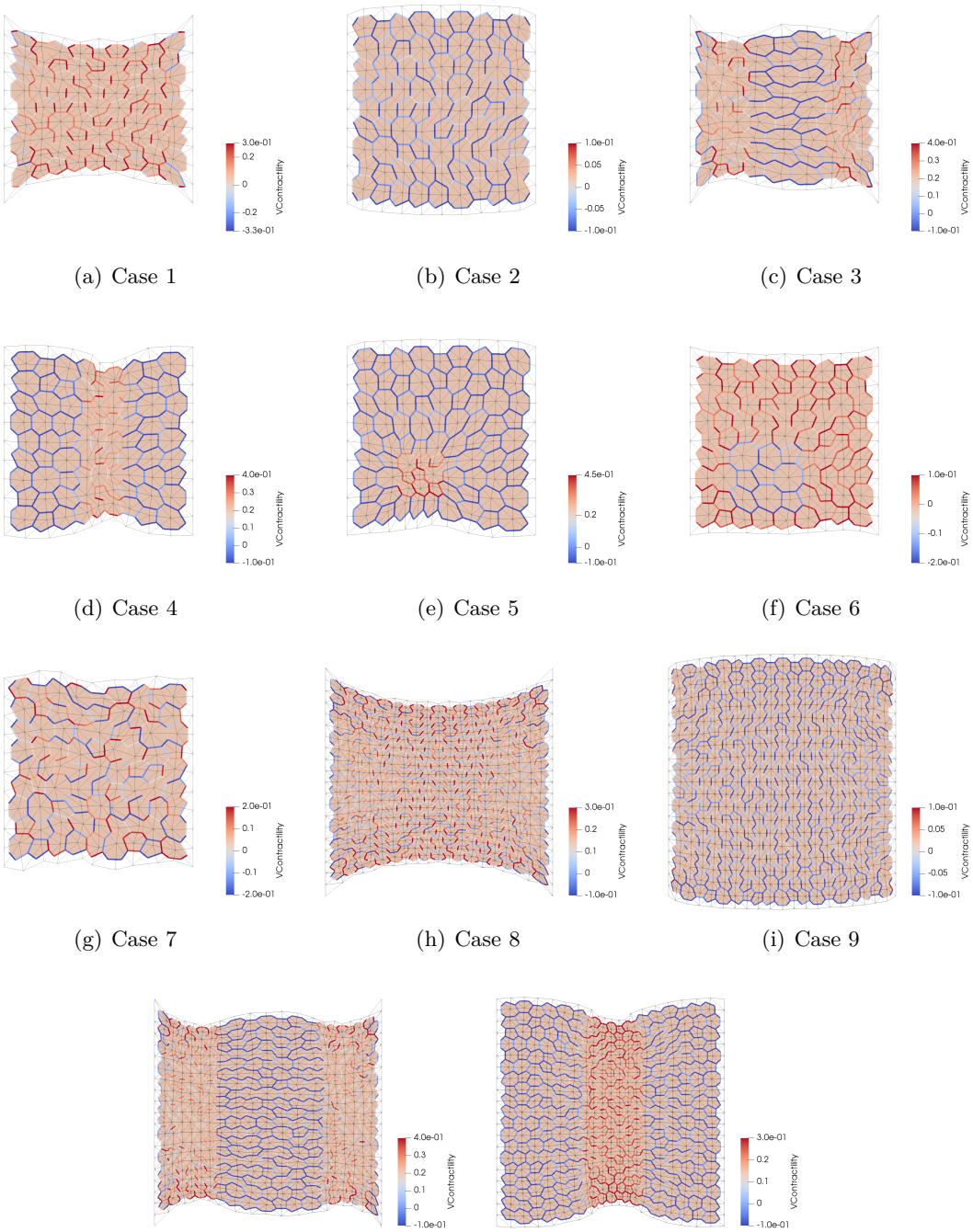

(a) Case 1 (b) Case 2 (c) Case 3

(d) Case 4 (e) Case 5 (f) Case 6

(g) Case 7 (h) Case 8 (i) Case 9

(j) Case 10 (k) Case 11

Figure 2.8: The resultant deformation after applying the contractions obtained using Least L_2**-norm** regularization (boundary is excluded in the inverse problem), the colored contours illustrate the obtained values of $\boldsymbol{\varepsilon}_c$, while the chosen numerical parameters were $k_D = 0.2$, $k_V = 1$ and $\lambda_A = 10$.

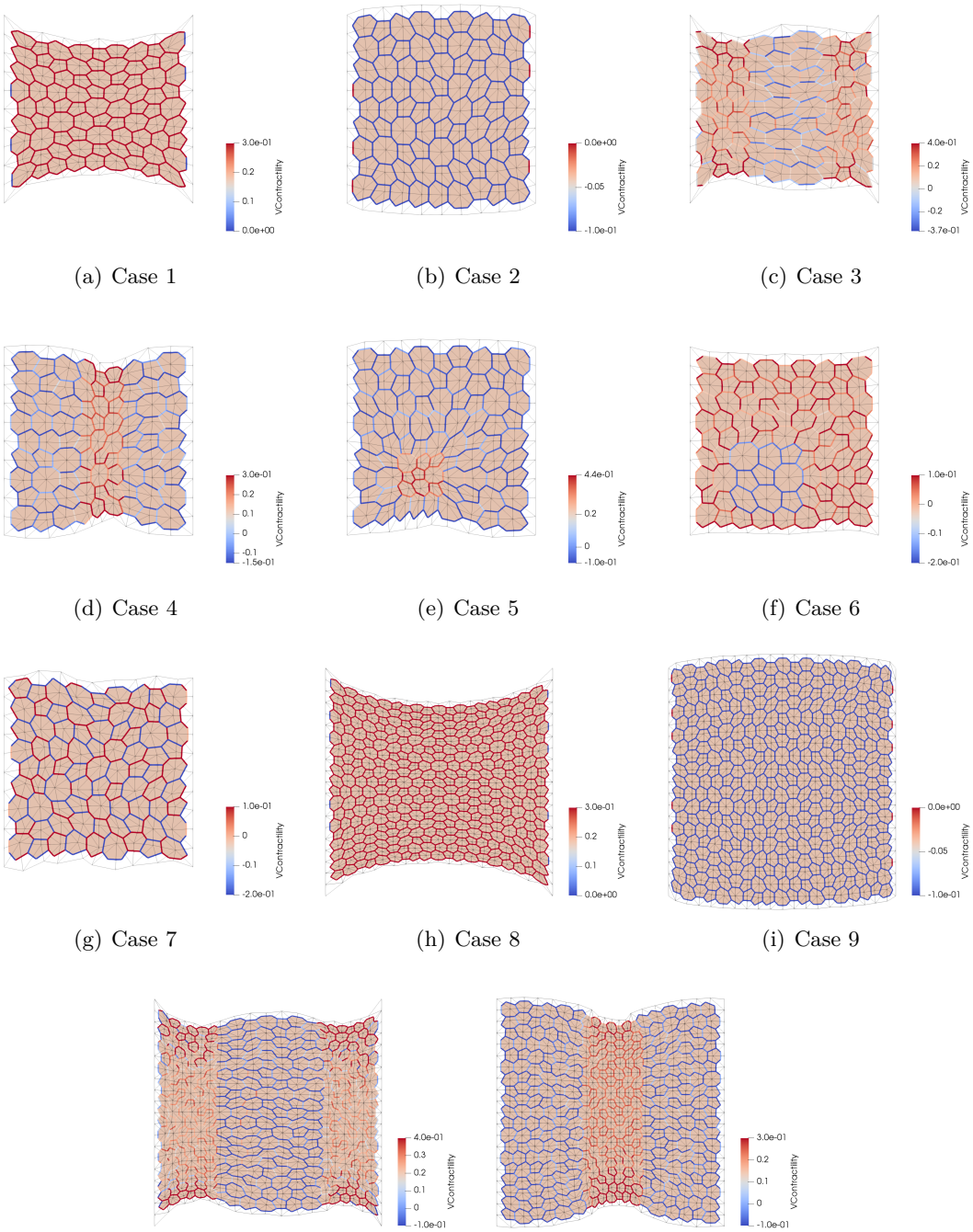

(a) Case 1 (b) Case 2 (c) Case 3

(d) Case 4 (e) Case 5 (f) Case 6

(g) Case 7 (h) Case 8 (i) Case 9

(j) Case 10 (k) Case 11

Figure 2.9: The resultant deformation after applying the contractions obtained using Least L_∞**-norm** regularization (boundary is excluded in the inverse problem), the colored contours illustrate the obtained values of $\boldsymbol{\varepsilon}_c$, while the chosen numerical parameters were $k_D = 0.2$, $k_V = 1$ and $\lambda_A = 10$.

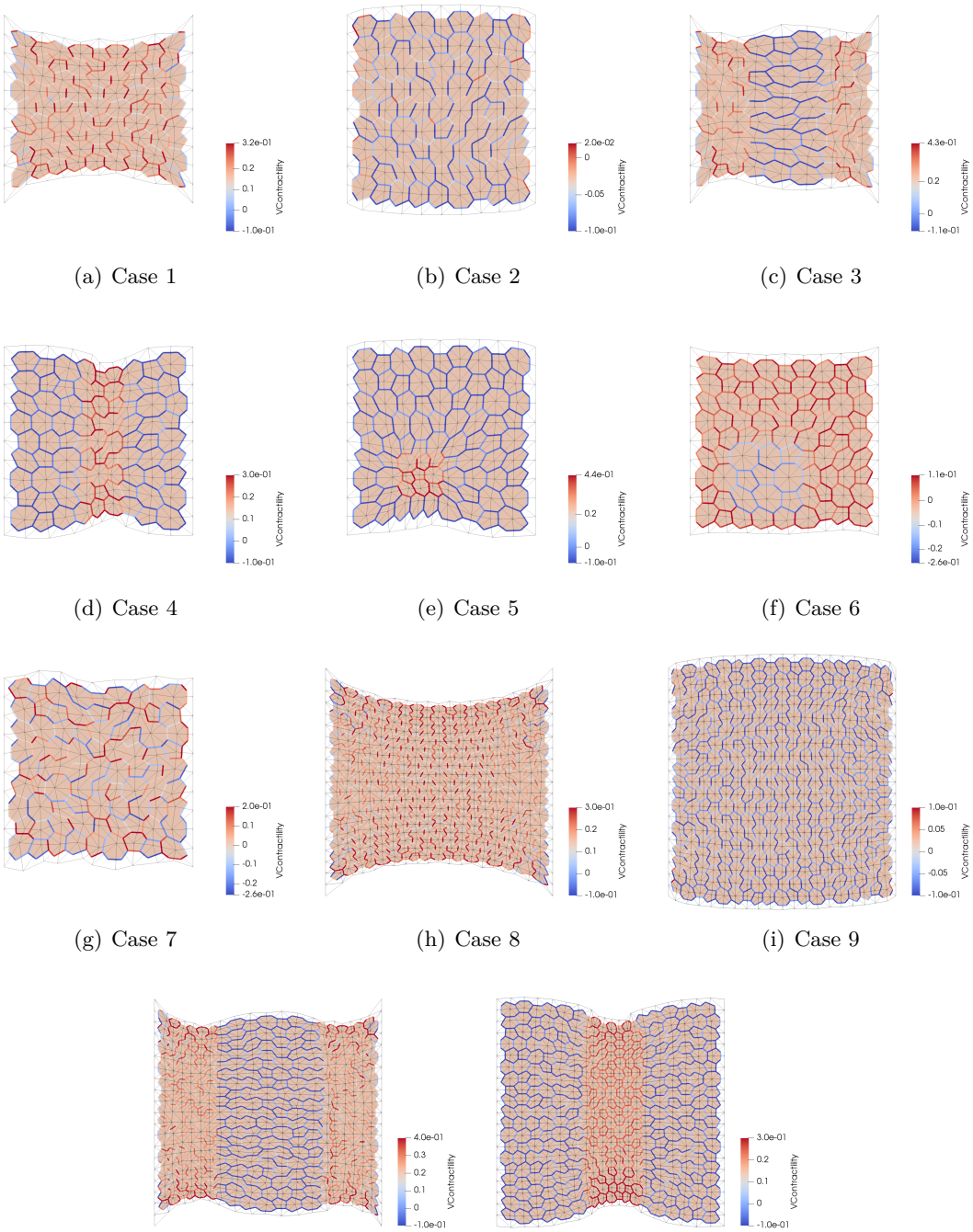

(a) Case 1 (b) Case 2 (c) Case 3

(d) Case 4 (e) Case 5 (f) Case 6

(g) Case 7 (h) Case 8 (i) Case 9

(j) Case 10 (k) Case 11

Figure 2.10: The resultant deformation after applying the contractions obtained using **minimum vertex residual** VR (boundary is excluded in the inverse problem), the colored contours illustrate the obtained values of $\boldsymbol{\varepsilon}_c$, while the chosen numerical parameters were $k_D = 0.2$, $k_V = 1$ and $\lambda_A = 10$

2.7.5 Homogeneous Contractility

In cases in which there is prior knowledge or prior assumption about the variation of contractility, the inverse problem may be modified by reducing the number unknowns based on the assumed distribution. In other words, bars that assumed to have the same values of ε_c can be presented by a single unknown instead of a assigning one unknown to each bar. This can be achieved by summing the columns of $\mathbf{K}_{x\varepsilon}$ which corresponds to the bars with same value of ε_c. The inverse problem defined in eq.(2.25), can be rewritten as,

$$\min_{\boldsymbol{\varepsilon_c}} \frac{1}{2}||\bar{\mathbf{K}}_{x\varepsilon}\bar{\boldsymbol{\varepsilon}}_c + \mathbf{q}_x||_2^2 \tag{2.47}$$

with $\bar{\mathbf{K}}_{x\varepsilon} \in \mathbb{R}^{2N_{nodes}\times N_c}$ having the same number of columns as the assumed variety of contractility N_c, such that each columns corresponds to the bars with value of ε_c

$$\bar{\mathbf{K}}_{x\varepsilon} = [\bar{\mathbf{K}}_{x\varepsilon 1}\ \bar{\mathbf{K}}_{x\varepsilon 2} \dots \bar{\mathbf{K}}_{x\varepsilon N_c}] \tag{2.48}$$

and the enters of each columns are

$$\bar{\mathbf{K}}^i_{x\varepsilon I} = \sum_l \mathbf{K}^{il}_{x\varepsilon} \tag{2.49}$$

where the summation extends to the set of bars l which are assumed to have the same value I of contractility. And the solution of the above problem can be obtained from the following linear system of equation

$$\bar{\mathbf{K}}^T_{x\varepsilon}\bar{\mathbf{K}}_{x\varepsilon}\bar{\boldsymbol{\varepsilon}}_c = \bar{\mathbf{K}}^T_{x\varepsilon}\mathbf{q}_x \tag{2.50}$$

Now, if we consider the set of cases in Figure 2.6 with a prior knowledge about the variation of $\boldsymbol{\varepsilon}_c$, the number of unknowns can be reduced by considering a single unknown for each set of equal contractions. For instance, in Case 1,2, 8 and 9 we consider a single unknown $N_c = 1$ with $\bar{\boldsymbol{\varepsilon}}_{\mathbf{c}} = \varepsilon_c^1 = \varepsilon_c^2 = \dots = \varepsilon_c^{N_V}$, while for Case 5 and 6 we consider two unknowns $N_c = 2$, one for the locally concentrated contractions and the other is for the rest of the tissue. As for Case 3, 4, 10 and 11 the problem is reduced to three unknowns $N_c = 3$ based on the vertical uniformity of $\boldsymbol{\varepsilon}_c$.

Figure 2.11 shows the relative error after the reduction of unknowns with and without area constraint, while the equalities corresponding to boundary nodes are excluded. Apparently, specifying the variation of ε_c makes the inverse problem well-defined enough to retrieve the exact values, even without including any information about the boundary. This might be an expected result, if we consider that fact that the significant reduction of unknown have converted the problem from being under-determined to over-determined with abundant information (equations).

From the small order of the error, it can be said that in this way we can retrieve the exact values of ε_c, but we remark, in these results the variation of ε_c is previously defined, therefore to consider this approach one should have a prior knowledge or introduce a hypothesis about the homogeneity of contractions.

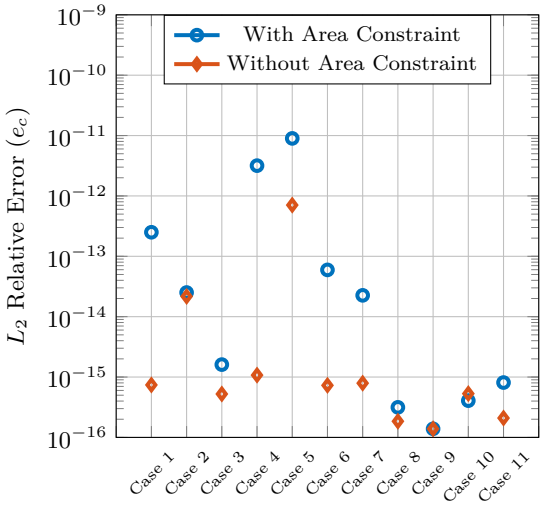

Figure 2.11: Relative error of the obtained contractions $\boldsymbol{\varepsilon}_c$, when the distribution of ε_c is unknown (Boundary is excluded).

Chapter 3

Inverse Analysis of Pure Vertex Model

In this chapter, we present briefly an extension of our analysis considering the case of purely vertex model in which cells are coupled through vertices only.

3.1 Model Topology

In case of a purely vertex model, the epithelial tissue is discretized to several polygons where each one represents a single cell. The boundary of cells is defined by set of vertices $\boldsymbol{y} = \{\boldsymbol{y}^1, \boldsymbol{y}^2, \ldots, \boldsymbol{y}^N\}$, with no extracellular space between cells, see Figure 3.1. The coupling between two neighboring vertices $\boldsymbol{y}^I$ and $\boldsymbol{y}^J$ is defined by one-dimensional bar elements which are presented by the dashed lines.

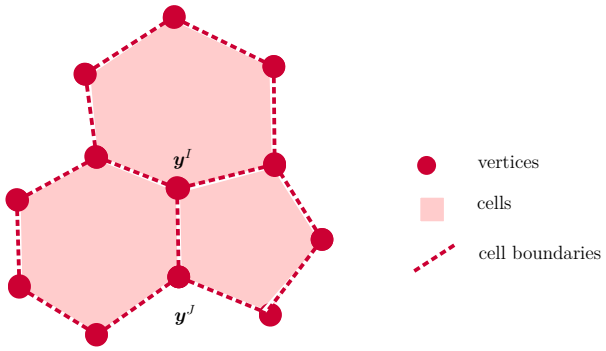

Figure 3.1: Discretisation of tissue into cells (polygons) and the cells boundaries (dashed lines) are defined by vertices, $\boldsymbol{y}^I$ (dots).

To generate the above defined discretization, we have used barycentric tessellation, following the same procedure as the Hybird model, section 2.1.

3.2 Rheological Model

To describe the bar elements connecting each pair of vertices IJ, we will consider an elastic rheological model with quadratic strain function.

$$W_V^{IJ}(\boldsymbol{y}) = \frac{1}{2} k_V (\varepsilon^{IJ})^2 L_0^{IJ} \qquad W_V(\boldsymbol{y}) = \sum_{IJ=1}^{N_V} W_V^{IJ}(\boldsymbol{y}) \tag{3.1}$$

with

$$\varepsilon^{IJ} = \varepsilon_e^{IJ} + \varepsilon_c^{IJ} \quad \varepsilon_e^{IJ} = \frac{l^{IJ} - L_0^{IJ}}{L_0^{IJ}} \quad l^{IJ} = ||\boldsymbol{y}^I - \boldsymbol{y}^J|| \quad L_0^{IJ} = ||\boldsymbol{y}_0^I - \boldsymbol{y}_0^J||$$

where k_V is the cell boundary stretching stiffness, and ε_e^{IJ} is the elastic strain measure of element IJ, with $L_0^{IJ}, l^I J$ being the current and reference lengths, respectively, and ε_c^{IJ} is the contractility of bar IJ.

3.3 Area Constraint

Same as the hybrid case, we have considered an additional energy term, to impose area constraint,

$$W_A = \frac{\lambda_A}{2} \sum_{m=1}^{N_{cell}} (A^m - A_0^m)^2 \tag{3.2}$$

where λ_A is a penalisation coefficient and A_0^m and A^m are the initial and the current areas of cell m, respectively.

Unlike the case of Hybrid model, the enforcement of area constraint is an essential part of pure vertex model, otherwise, it might show unrealistic behavior in which cell size is reduced significantly.

3.4 Mechanical Equilibrium

The mechanical equilibrium of the bar elements of the purely vertex network is obtained by minimizing the total energy $W_V(\boldsymbol{y}) + W_A(\boldsymbol{y})$ considering the principal kinematic variable $\boldsymbol{y}$

$$\frac{\partial W_V(\boldsymbol{y})}{\partial \boldsymbol{y}^I} + \frac{\partial W_A(\boldsymbol{y})}{\partial \boldsymbol{y}^I} = \mathbf{0}, \quad I = 1, \ldots, N_{vertices} \tag{3.3}$$

which also can be interpreted as the force equilibrium at each vertex such that,

$$\mathbf{g}_y^I := \mathbf{g}_V^I + \mathbf{g}_A^I = \mathbf{0}, \quad i = 1, \ldots, N_{vertives} \tag{3.4}$$

with $\mathbf{g}_V^I$ is summation of tractions at vertex I due to the bars connecting with neighboring vertices S^I

$$\mathbf{g}_V^I := \sum_{J \in S^I} \frac{\partial W_V^{IJ}}{\partial \boldsymbol{y}^I} = \sum_{J \in S^I} \frac{\partial W_V^{IJ}}{\partial \boldsymbol{y}^I} = \sum_{J \in \mathcal{S}^I} k_V \, \varepsilon^{IJ} \, \mathbf{e}^{IJ} \tag{3.5}$$

while $\mathbf{g}_A^I$ is area contribution on vertex I

$$\mathbf{g}_A^I := \frac{\partial W_A}{\partial \boldsymbol{y}^I} = \frac{\lambda_A}{2} \mathbf{J} \sum_{m=\bar{S}^I} (A^m - A_0^m) \sum_{KL \in P^m} (\boldsymbol{y}^L \delta_{KI} - \boldsymbol{y}^K \delta_{IL}) \tag{3.6}$$

where the notation δ_{KI} refers to Kronecker delta, and $\bar{S}^I$ are the three cells which are coupled through vertex I.

Then, the total mechanical equilibrium of the system can be expressed by the set of the following nonlinear equations

$$\mathbf{g}_y(\boldsymbol{y}, \boldsymbol{\varepsilon}_c) = \mathbf{0} \tag{3.7}$$

where

$$\mathbf{g}_y^I = \sum_{J \in \mathcal{S}^I} k_V \, \varepsilon^{IJ} \, \mathbf{e}^{IJ} + \frac{\lambda_A}{2} \mathbf{J} \sum_{m=\bar{S}^I} (A^m - A_0^m) \sum_{KL \in P^m} (\boldsymbol{y}^L \delta_{KI} - \boldsymbol{y}^K \delta_{IL}) \tag{3.8}$$

3.5 Direct Problem

For a given set of contractions $\boldsymbol{\varepsilon}_c = \{\varepsilon_c^1, \varepsilon_c^2, ..., \varepsilon_c^{N_V}\}$ obtain the position of vertices $\boldsymbol{y} = \{\boldsymbol{y}^1, \ldots, \boldsymbol{y}^{N_{vertices}}\}$ that minimize the total energy, which basically involve solving the set of nonlinear equations in (3.7) for $\boldsymbol{y}$, Newton's method can be written as

$$\Delta \boldsymbol{y}^{k+1} = -(\mathbf{K}_{yy}(\boldsymbol{y}^k))^{-1} \, \mathbf{g}_y(\boldsymbol{y}^k) \tag{3.9}$$

Where $\mathbf{K}_{yy} \in \mathbb{R}^{2N_{vertices} \times 2N_{vertices}}$ is the Jacobian matrix with enters of the following partial derivatives

$$\mathbf{K}_{yy}^{IJ} = \frac{\partial \mathbf{g}_y^I}{\partial \boldsymbol{y}^J} = \frac{\partial \mathbf{g}_V^I}{\partial \boldsymbol{y}^J} + \frac{\partial \mathbf{g}_A^I}{\partial \boldsymbol{y}^J} \tag{3.10}$$

with

$$\begin{aligned}
\frac{\partial \mathbf{g}_V^I}{\partial \boldsymbol{y}^J} &= \sum_{J \in \mathcal{S}^I} \mathbf{K}_t^{IJ} \\
\frac{\partial \mathbf{g}_A^I}{\partial \boldsymbol{y}^J} &= \frac{\lambda_A}{2} \mathbf{J} \sum_{m=\bar{S}^I} (A^m - A_0^m) \sum_{KL \in P^m} (\delta_{KI}\delta_{LJ}\mathbf{I} - \delta_{IL}\delta_{JK}\mathbf{I}) \\
&\quad + \frac{\lambda_A}{4} \sum_{m=\bar{S}^I} \sum_{KL \in P^m} \mathbf{J}(\boldsymbol{y}^L \delta_{KI} - \boldsymbol{y}^K \delta_{IL}) \otimes \sum_{NM \in P^m} \mathbf{J}(\boldsymbol{y}^M \delta_{NJ} - \boldsymbol{y}^N \delta_{JM}),
\end{aligned}$$

3.6 Inverse Problem

For a given set of vertex position $\boldsymbol{y} = \{\boldsymbol{y}^I, \ldots, \boldsymbol{y}^{N_{vertices}}\}$ obtain the contractility vector $\boldsymbol{\varepsilon}_c = \{\varepsilon_c^1, \varepsilon_c^2, ..., \varepsilon_c^{N_V}\}$ that satisfy the mechanical equilibrium defined in eq.(3.7), which can be written in least-square format as

$$\min_{\boldsymbol{\varepsilon_c}} \frac{1}{2} ||\mathbf{g}_y(\boldsymbol{\varepsilon}_c)||_2^2 \tag{3.11}$$

and since the residual vector $\mathbf{g}_y$ depends linearly on $\boldsymbol{\varepsilon}_c$ it can be decoupled as

$$\min_{\boldsymbol{\varepsilon_c}} \frac{1}{2} ||\mathbf{K}_{y\varepsilon}\boldsymbol{\varepsilon}_c + \mathbf{q}_y||_2^2 \tag{3.12}$$

where $\mathbf{K}_{y\varepsilon} \in \mathbb{R}^{2N_{vertices} \times N_V}$ and $\mathbf{q}_x \in \mathbb{R}^{2N_{vertices}}$ having the following entries,

$$\mathbf{K}_{y\varepsilon}^{I,IJ} = k_V \boldsymbol{e}^{IJ} \qquad \mathbf{q}_y^I = \sum_{J \in \mathcal{S}^I} k_V \varepsilon_e^{IJ} \boldsymbol{e}^{IJ} + \mathbf{g}_A^I \tag{3.13}$$

In the above problem considering minimal L_2-norm as an objective is sufficient to insure the uniqueness of the problem. Based on the fact that the column space of $\mathbf{K}_{y\varepsilon}$ tend to be larger than the row space (see Figure 2.3), which basically implies that our mechanical equilibrium is characterized by having more equalities ($2N_{vertices}$) then unkowns (N_V). The solution can be obtained from the following linear system of equations.

$$\nabla_{\boldsymbol{\varepsilon}_c} \big(\frac{1}{2} ||\mathbf{K}_{y\varepsilon}\boldsymbol{\varepsilon}_c + \mathbf{q}_y||_2^2 \big) = 0 \tag{3.14}$$

$$\mathbf{K}_{y\varepsilon}^T \mathbf{K}_{y\varepsilon} \boldsymbol{\varepsilon}_c = -\mathbf{K}_{y\varepsilon}^T \mathbf{q}_y \tag{3.15}$$

this also can be seen as uisng *MoorePenrose right* pseudoinverse $\mathbf{K}_{y\varepsilon}^{\dagger} = (\mathbf{K}_{y\varepsilon}^T \mathbf{K}_{y\varepsilon})^{-1} \mathbf{K}_{y\varepsilon}^T$.

3.7 Numerical Experiments

To check the validity of the inverse problem, we followed the same approach as in the case of Hybrid model, by testing the compatibility between the direct and inverse problems, first, we solve a direct problem with a prescribed set of contractilitiy ε_c, then from the deformed configuration, we solve an inverse problem to retrieve those contractions ε. In contrast to the Hybrid model, here we take the position of vertices $\boldsymbol{y}$ as input for the inverse problem.

As a case study we considered to two initial configuration identical to the one used in the previous chapter (see Figure 3.2). Then, 6 deformed configuration were generated, by solving direct problem while fixing the vertices on the left and right boundaries. Figure 3.3 shows the resultant deformation with the prescribed values of ε_c. As it might

be noticed, the bars which are located in the boundary are always assumed to have zero contractions. This is because when we exclude boundary vertices in the inverse problem, the contraction ε_c corresponding to these bars will not be included in any equality, thus they need to excluded from the linear system, so to have a comparable results we assign zero contraction from them.

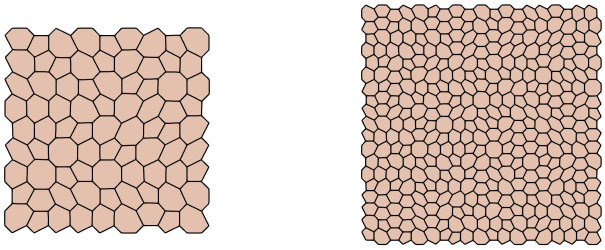

(a) 10×10 (b) 20×20

Figure 3.2: The initial configuration of 10×10 and 20×20 tissues, respectively, with fixed vertices at the left and right edges.

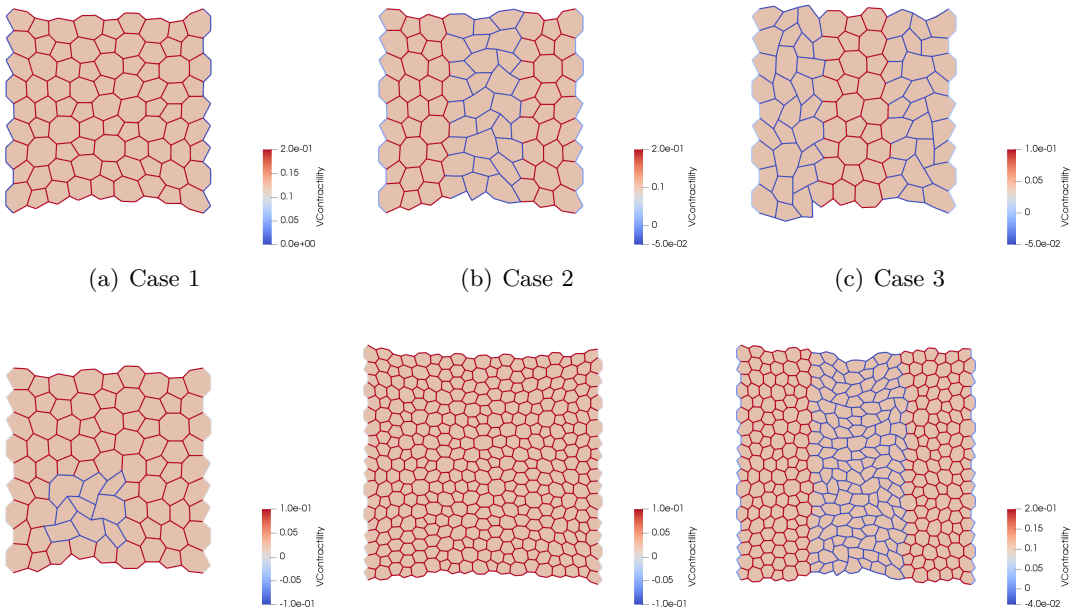

(a) Case 1 (b) Case 2 (c) Case 3

(d) Case 4 (e) Case 5 (f) Case 6

Figure 3.3: Different deformed tissues used as an input for inverse analysis, the colored contours illustrate the prescribed values of $\boldsymbol{\varepsilon}$, while the chosen numerical parameters were $k_V = 5$ and $\lambda_A = 10$.

During these numerical experiments, we observed that the feasibility of the direct problem is not always guaranteed. The quadratic convergence of Netwon's method was deficient, while in many cases the method diverges without line search, especially those with negative contractility (expansion). This suggests that in these situations our solver is not able to find a global minimal. For example, in case 2, 3, 4 and 6, convergence was only achieved after we sought for the local minimal by reducing the step size by 1/10, which of course demanded high number of iteration with an average or 300 iterations.

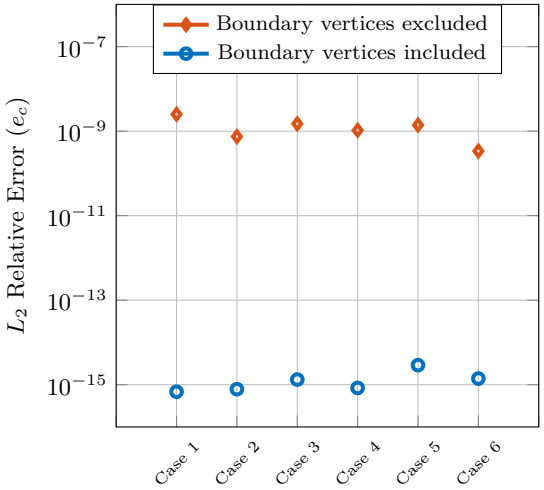

Figure 3.4: Relative error of the obtained contractions ε_c, in case of purely vertex model.

On the other hand, the inverse problem is well-defined. The relative error associated to the solution of the inverse problem is shown in Figure 3.4. It appears that taking equilibrium at the vertices, while considering a least-square problem is sufficient to identify the contractility even when the boundary is eliminated, while if it is included we retrieve the exact values.

Chapter 4

Inverse Analysis of Wound Healing

In the following chapter, we present the inverse analysis carried out to infer the contraction that drive wound healing, using hybrid cell-center/vertex model.

4.1 Introduction

Modeling a wound healing process in monolayers requires major modification to the hybrid cell-center/vertex model. As pointed in section section 2.1, vertices and cell-centred positions are coupled through the constraint in eq.(2.1), which leads to mechanical equilibrium in which the summation of forces vanishes only on nodes. But, when it comes wound healing, this type of equilibrium provide unrealistic behavior, in which the wound edge takes a zig-zag shape see Figure 4.1.

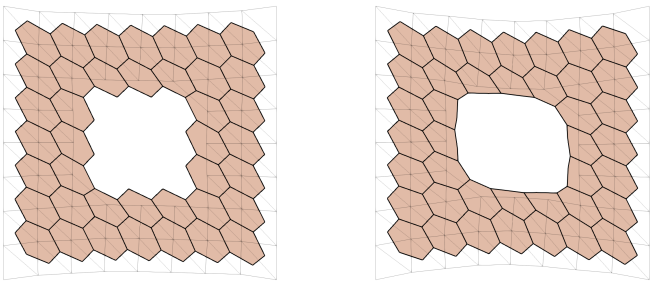

(a) Without y-relaxation (b) With y-relaxation

Figure 4.1: The effect of relaxing vertices during wound closure. (a) Deformed tissue without y-relaxation. (b) Deformed tissue when wound vertices are relaxed.

In order to avoid these effects, the constraint in eq.(2.1) is disregarded for those vertices at the wound edge $\boldsymbol{y}_w = \{\boldsymbol{y}_w^1, \boldsymbol{y}_w^2, \ldots, \boldsymbol{y}_w^{N_w}\}$, instead they are allowed to change their position independently. In this case, mechanical equilibrium is expressed as a vanishing sum of tractions at nodes and wounded vertices (Section 4.2) .

Now, inverting the mechanical equilibrium arises major challenge regarding the position of vertices at the wound edge. These positions are no longer defined in term of nodel positions, while extracting them form a experimental images can be more challenging, due to the highly dynamic behavior of cell membrane. Instead, we have considered an iterative approach in which wounded vertices are regarded as unknowns. And our only inputs that are extracted form images are the sequential configurations of cell centers $\boldsymbol{x}$ and the evolution of the area of the wound A_w^*.

Problem Statement

The problem of wound healing can be stated as, for a given set of nodal positions (cell centers) $\boldsymbol{x} = \{\boldsymbol{x}^1, \ldots, \boldsymbol{x}^{N_{nodes}}\}$ and wounded area A_w^* obtained the position of vertices at wound edge $\boldsymbol{y}_w = \{\boldsymbol{y}_w^1, \boldsymbol{y}_w^2, \ldots, \boldsymbol{y}_w^{N_w}\}$ and the contractilitiy $\boldsymbol{\varepsilon}_c$ that satisfy the mechanical equilibrium.

To solve the problem we have considered two-step iterative approach, as shown in Figure 4.2, in one step we solve a particularized direct problem for vertices $\boldsymbol{y}_w$ (Section 4.3.1) in which we impose the area of the wound A_w^*, while in second step we compute the values of $\boldsymbol{\varepsilon}_c$ by solving an inverse problem (Section 4.4). Furthermore, as a convergence criteria we have considered the increment of $\boldsymbol{y}_w$, such we keep iterating between the two steps as long as $\Delta \boldsymbol{y}_w$ is larger then a prescribed tolerance.

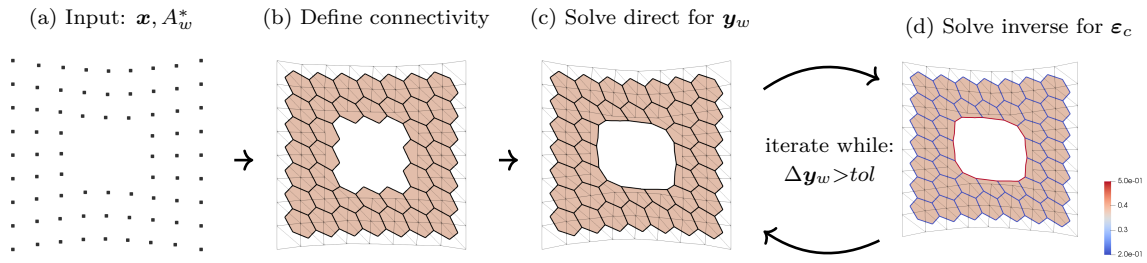

Figure 4.2: Flow chart shows the iterative procedure to approximate contractility during wound healing. (a) Input: nodal displacement $\boldsymbol{x}$ and wound Area A_w^*. (b) Applying barycentric tessellation to define the connectivity of tissue. (c) Solving dierct problem for the position of wounded vertices $\boldsymbol{y}_w$ while imposing the area of wound. (d) Solving inverse problem for contractility ε_c.

4.2 Mechanical Equilibrium with y_w-relaxation

The extension of the system with addition Degrees-of-freedom $\boldsymbol{y}_w$ modifies the minimization problem in eq.(2.11), which now takes the from

$$\{\boldsymbol{x}, \boldsymbol{y}_w\} = \text{argmin}_{\boldsymbol{x},\boldsymbol{y}_w} W(\boldsymbol{x}, \boldsymbol{y}_w) \tag{4.1}$$

Furthermore, to prevent large displacement of $\boldsymbol{y}_m$ and minimize discontinuities between sequential deformations, an addition energy term W_R is added to the system, such that it penalizes the variation of $\boldsymbol{y}_m$,

$$W_R(\boldsymbol{y}_w) = \frac{\lambda_y}{2} \sum_{I=1}^{N_w} ||\boldsymbol{y}_w^I - \boldsymbol{y}_{w0}^I||^2 \tag{4.2}$$

where the notation $\boldsymbol{y}_{w0}$ indicate the position of vertices at the previous configuration. In the more general case this energy term is equivalent to a viscous-like-effect, while the factor λ_y is taken as a viscous coefficient that varies with time step $\lambda_y \approx \frac{\eta}{\Delta t}$.

Taking into account the above additional energy the total energy will be:

$$W(\boldsymbol{x}, \boldsymbol{y}_w) = W_D(\boldsymbol{x}) + W_V(\boldsymbol{y}(\boldsymbol{x}), \boldsymbol{y}_w) + W_A(\boldsymbol{x}, \boldsymbol{y}_w) + W_R(\boldsymbol{y}_w) \tag{4.3}$$

And equilibrium is now represented by two systems of equations,

$$\mathbf{g} := \begin{Bmatrix} \mathbf{g}_x \\ \mathbf{g}_y \end{Bmatrix} = \mathbf{0} \tag{4.4}$$

with $\mathbf{g}_x = \nabla_x W(\boldsymbol{x}, \boldsymbol{y}_w)$ and $\mathbf{g}_y = \nabla_{y_w} W(\boldsymbol{x}, \boldsymbol{y}_w)$, are the residual vectors with the contributions corresponds to each node $\boldsymbol{x}$ and wounded vertex $\boldsymbol{y}_w$,

$$\mathbf{g}_x^i := \frac{\partial W(\boldsymbol{x}, \boldsymbol{y}_w)}{\partial \boldsymbol{x}^i} = \mathbf{g}_D^i + \mathbf{g}_V^i + \mathbf{g}_A^i \quad i = 1, 2, \ldots, N_{nodes} \tag{4.5}$$

$$\mathbf{g}_y^I := \frac{\partial W(\boldsymbol{x}, \boldsymbol{y}_w)}{\partial \boldsymbol{y}_w^I} = \mathbf{g}_V^I + \mathbf{g}_A^I + \mathbf{g}_R^I \quad I = 1, 2, \ldots, N_w \tag{4.6}$$

where the contribution coming from y-relaxation can be written as

$$\mathbf{g}_R^I = \frac{\partial W_R(\boldsymbol{y}_w)}{\partial \boldsymbol{y}_w^I} = \lambda_{y_w}(\boldsymbol{y}_w^I - \boldsymbol{y}_{w0}^I) \tag{4.7}$$

while the expressions of $\mathbf{g}_D^i$, $\mathbf{g}_V^i$, $\mathbf{g}_A^i$,$\mathbf{g}_V^I$ and $\mathbf{g}_A^I$ can be found in Section 2.4 and 3.4.

Remark: we remark that all the notation in this chapter indicate that the same expressions as those derived in the previous chapters, except that the coupling between wounded vertices and nodes is disregarded. Practically, this can be achieved easily, one can consider using the same implementation while setting the interpolation function equals to zero, such that

$$N^i(\boldsymbol{\xi}^I) = 0, \qquad \forall i \in \boldsymbol{x}, \quad \forall I \in \boldsymbol{y^w}, \tag{4.8}$$

4.3 Direct problem

The general direct problem of wound healing can be stated as, for a given set of contractions $\boldsymbol{\varepsilon}_c = \{\varepsilon_c^1, \varepsilon_c^2, ..., \varepsilon_c^{N_V}\}$ obtain the set of nodal positions $\boldsymbol{x} = \{\boldsymbol{x}^1, \ldots, \boldsymbol{x}^{N_{nodes}}\}$ and the position of wounded vertices $\boldsymbol{y}_w = \{\boldsymbol{y}_w^1, \boldsymbol{y}_w^2, \ldots, \boldsymbol{y}_w^{N_w}\}$ such that the mechanical equilibrium defined previous section is satisfied, which involve solving the set of nonlinear system of equations in (4.4).

$$\mathbf{g} := \begin{Bmatrix} \mathbf{g}_x(\boldsymbol{z}) \\ \mathbf{g}_y(\boldsymbol{z}) \end{Bmatrix} = \mathbf{0} \qquad \boldsymbol{z} = \begin{Bmatrix} \boldsymbol{x} \\ \boldsymbol{y}^w \end{Bmatrix} \tag{4.9}$$

Taking $\boldsymbol{z}$ as combined vector of unknowns with position of nodes and wounded vertices, Newton's method can be written as

$$\Delta \boldsymbol{z}^{k+1} = -(\mathbf{K}_{\boldsymbol{z}}(\boldsymbol{z}^k))^{-1}\ \mathbf{g}(\boldsymbol{z}^k) \tag{4.10}$$

with $\mathbf{K}_z \in \mathbb{R}^{(2N_{nodes}+2N_w)\times(2N_{nodes}+2N_w)}$ being the Jacobian which takes the following form

$$\mathbf{K}_z = \begin{bmatrix} \mathbf{K}_{xx} & \mathbf{K}_{xy} \\ \mathbf{K}_{yx} & \mathbf{K}_{yy} \end{bmatrix} \tag{4.11}$$

with

$$\mathbf{K}_{xx}^{ij} = \frac{\partial \mathbf{g}_D^i}{\partial \boldsymbol{x}^j} + \frac{\partial \mathbf{g}_V^i}{\partial \boldsymbol{x}^j} + \frac{\partial \mathbf{g}_A^i}{\partial \boldsymbol{x}^j} \qquad \mathbf{K}_{xy}^{iJ} = \frac{\partial \mathbf{g}_V^i}{\partial \boldsymbol{y}_w^J} + \frac{\partial \mathbf{g}_A^i}{\partial \boldsymbol{y}_w^J}$$

$$\mathbf{K}_{yx}^{Ij} = \frac{\partial \mathbf{g}_V^I}{\partial \boldsymbol{x}^j} + \frac{\partial \mathbf{g}_A^I}{\partial \boldsymbol{x}^j} \qquad \mathbf{K}_{yy}^{IJ} = \frac{\partial \mathbf{g}_V^I}{\partial \boldsymbol{y}_w^J} + \frac{\partial \mathbf{g}_A^I}{\partial \boldsymbol{y}_w^J} + \frac{\partial \mathbf{g}_R^I}{\partial \boldsymbol{y}_w^J}$$

$$\mathbf{K}_{xy}^{iJ} = \frac{\partial^2 (W_V + W_A)}{\partial \boldsymbol{x}^i \partial \boldsymbol{y}_w^J} = \left[\frac{\partial^2 (W_V + W_A)}{\partial \boldsymbol{y}_w^I \partial \boldsymbol{x}^j}\right]^T = \mathbf{K}_{yx}^{Ij\,T}$$

$$\frac{\partial \mathbf{g}_A^i}{\partial \boldsymbol{y}_w^J} = \frac{\lambda_A}{2}\mathbf{J} \sum_{m\in\bar{S}^i} (A^m - A_0^m) \sum_{IK\in P^m} \left(N^i(\boldsymbol{\xi}^I)\delta_{KJ}|_{I\notin \boldsymbol{y}_w} - N^i(\boldsymbol{\xi}^J)\delta_{IJ}|_{J\notin \boldsymbol{y}_w}\right)$$
$$+ \frac{\lambda_A}{4} \sum_{m\in\bar{S}^i} \sum_{IK\in P^m} (\boldsymbol{y}^K\delta_{IJ} - \boldsymbol{y}^I\delta_{KJ}) \otimes \sum_{IK\in P^m} \left(N^i(\boldsymbol{\xi}^I)\boldsymbol{y}^K|_{I\notin \boldsymbol{y}_w} - N^i(\boldsymbol{\xi}^K)\boldsymbol{y}^I|_{K\notin \boldsymbol{y}_w}\right)$$

$$\frac{\partial \mathbf{g}_R^I}{\partial \boldsymbol{y}_w^J} = \lambda_y \mathbf{I}$$

The terms which are not included here can be found in section 2.5 and 3.5.

4.3.1 Direct problem with an imposed wound area A_w^*

As mention earlier, we want to avoid tracking the position of wounded vertices $\boldsymbol{y}_w$ during our inverse analysis, instead we obtain them by solving a particularized direct problem in which we impose the area of the wound. This problem can be stated as; for a given set of cell centers $\boldsymbol{x} = \{\boldsymbol{x}^1, \ldots, \boldsymbol{x}^{N_{nodes}}\}$, contractions $\boldsymbol{\varepsilon}_c = \{\varepsilon_c^1, \varepsilon_c^2, ..., \varepsilon_c^{N_V}\}$ and the area of the wound A_w^*, obtain the set on wounded vertices $\boldsymbol{y}_w = \{\boldsymbol{y}_w^1, \boldsymbol{y}_w^2, \ldots, \boldsymbol{y}_w^{N_w}\}$ that satisfy equilibrium.

Firstly, we introduce an additional energy term that enforces the area of the wound using the same fashion that have been used for cell area constraint

$$W_w(\boldsymbol{y}_w) = \frac{\lambda_w}{2}(A_w - A_w^*) \tag{4.12}$$

where λ_w is a penalty parameter, A_w is the current wound area, and A_w^* is the exact wound area which is extracted form experimental images. In order to obtain the expression of A_w, one may consider the same steps that have been applied for the area of a single cell (see section 2.3), which will lead to

$$A_w = \frac{1}{2} \sum_{IJ \in P^w} \boldsymbol{y}_w^I . \mathbf{J} \boldsymbol{y}_w^J \tag{4.13}$$

while here P^w refers to the segments of polygon that defines wound ring.

Then, the equilibrium is modified by including the greadient of the above energy term, such that,

$$\mathbf{g}_y = \mathbf{0} \tag{4.14}$$

with

$$\bar{\mathbf{g}}_y^I(\boldsymbol{y}_w) := \mathbf{g}_V^I + \mathbf{g}_A^I + \mathbf{g}_R^I + \mathbf{g}_w^I \quad I = 1, 2, \ldots, N_w$$

$$\mathbf{g}_w^I = \frac{\partial W_w(\boldsymbol{y}_w)}{\partial \boldsymbol{y}_w^I} = \frac{\lambda_w}{2} \mathbf{J}(A_w - A_w^*) \sum_{KL \in P^w} (\boldsymbol{y}^L \delta_{KI} - \boldsymbol{y}^K \delta_{IL})$$

Similarly, the position of vertices $\boldsymbol{y}_w$ is obtained by solving the above nonlinear system using Newton's method, which arises the linearization of the additional penalty term, that takes the following form,

$$\frac{\partial \mathbf{g}_w^I}{\partial \boldsymbol{y}_w^J} = \frac{\lambda_w}{2} \mathbf{J}(A_w - A_w^*) \sum_{KL \in P^w} (\delta_{KI}\delta_{LJ}\mathbf{I} - \delta_{IL}\delta_{JK}\mathbf{I}) \tag{4.15}$$

$$+ \frac{\lambda_A}{4} \sum_{KL \in P^w} \mathbf{J}(\boldsymbol{y}_w^L \delta_{KI} - \boldsymbol{y}_w^K \delta_{IL}) \otimes \sum_{NM \in P^w} \mathbf{J}(\boldsymbol{y}_w^M \delta_{NJ} - \boldsymbol{y}_w^N \delta_{JM}) \tag{4.16}$$

4.4 Inverse problem

As shown in Figure 4.2, the values of contractility are corrected iteratively with the direct problem in which we enforce the area of wound A_w^*, therefore, we can state the inverse problem as; for a given set of nodal positions $\boldsymbol{x} = \{\boldsymbol{x}^1, \ldots, \boldsymbol{x}^{N_{nodes}}\}$ and corrected set of wounded vertices $\boldsymbol{y}_w = \{\boldsymbol{y}_w^1, \boldsymbol{y}_w^2, \ldots, \boldsymbol{y}_w^{N_w}\}$ obtain the corresponding values of contractions $\boldsymbol{\varepsilon}_c$ that satisfy the mechanical equilibrium in Section 4.2.
The problem can be written in a least-squares format,

$$\min_{\varepsilon_c} \frac{1}{2} ||\mathbf{g}(\boldsymbol{\varepsilon}_c)||_2^2 \tag{4.17}$$

the residual vector can be decoupled in matrix from, such as

$$\min_{\varepsilon_c} \frac{1}{2} ||\mathbf{K}_{z\varepsilon}\ \boldsymbol{\varepsilon}_c + \mathbf{q}_z||_2^2 \tag{4.18}$$

with

$$\mathbf{K}_{z\varepsilon} = \begin{bmatrix} \mathbf{K}_{x\varepsilon} \\ \mathbf{K}_{y\varepsilon} \end{bmatrix} \qquad \mathbf{q}_z = \begin{bmatrix} \mathbf{q}_x \\ \mathbf{q}_y + \mathbf{g}_R \end{bmatrix}$$

expressions for $\mathbf{K}_{x\varepsilon}$, $\mathbf{K}_{x\varepsilon}$,$\mathbf{q}_x$ and $\mathbf{q}_y$ can be found in eq.(2.26), (2.27) and (3.13), respectively.

As it might be noticed, the penalty term which imposes wound area A_w^* is not included when we compute the contractility, instead, we compute it from the original mechanical equilibrium in eq.(4.4). Therefore, the step in which we solve a direct problem while we enforce the wound area A_w^* can be seen as nothing but a geometrical correction of fitting operation in which we obtianed the position of vertices based on the wound area.
During the period from cell ablation until the closure of the wound, we will assumed that tissue goes through two different phases:

4.4.1 Expansion-Phase

Here we refer to the period that immediately follows ablation, in which cells surrounding the wound usually retract outwardly [64]. In this phase, we are assuming homogenouse contractility such that $\boldsymbol{\varepsilon_c} = \varepsilon_c^1 = \varepsilon_c^2 \ldots = \varepsilon_c^{N_V}$, this allows to reduce the problem in eq.(4.18) to one equations with single unknown,

$$\bar{\mathbf{K}}_{z\varepsilon}^T \bar{\mathbf{K}}_{z\varepsilon} \varepsilon_c = \bar{\mathbf{K}}_{z\varepsilon}^T \mathbf{q}_z \tag{4.19}$$

with $\bar{\mathbf{K}}_{z\varepsilon} \in \mathbb{R}^{2N_{nodes}+2N_w}$ such that,

$$\bar{\mathbf{K}}_{z\varepsilon}^I = \sum_J \mathbf{K}_{z\varepsilon}^{IJ} \tag{4.20}$$

where the summation in the above expression extends to the whole columns of $\mathbf{K}_{z\varepsilon}$.

4.4.2 Closure-Phase

After tissue retraction, actomyosin ring start to assemble at wound margin, whose contractions drives the wound edges together like a purse-string [64]. Therefore, in this phase we are considering two values of contractions, one for those bars that are at the wound edge, and the other is for the rest of the tissue, the least-squares problem in eq.(4.18) will be

$$\left[\bar{\mathbf{K}}_{z\varepsilon 1}\ \bar{\mathbf{K}}_{z\varepsilon 2}\right]^T \left[\bar{\mathbf{K}}_{z\varepsilon 1}\ \bar{\mathbf{K}}_{z\varepsilon 2}\right] \begin{bmatrix} \varepsilon_c^t \\ \varepsilon_c^w \end{bmatrix} = \left[\bar{\mathbf{K}}_{z\varepsilon 1}\ \bar{\mathbf{K}}_{z\varepsilon 2}\right]^T \mathbf{q}_z \tag{4.21}$$

with

$$\bar{\mathbf{K}}^I_{z\varepsilon 1} = \sum_J^{tissue} \mathbf{K}^{IJ}_{z\varepsilon} \qquad \bar{\mathbf{K}}^I_{z\varepsilon 2} = \sum_L^{wound} \mathbf{K}^{IL}_{z\varepsilon} \tag{4.22}$$

such that L extends over the columns corresponding to the wounded bars and J extends over the rest of the tissue.

4.5 Wound Healing Analysis

All the above formulation were implemented in *Matlab R2016a*, such that we have created a particular solver of each problem that are stated previously. In this section we shown the assessment of our implementation through numerical tests along with the results obtained based on experimental data.

4.5.1 Numerical Experiments

Same as in the previous chapters, we assessed our iterative approach, by checking the compatibility with the direct problems. Figure 4.3 shows a manufactured wound healing by solving direct problem (Section 4.3) with prescribed contractions ($\boldsymbol{\varepsilon}_c^t = 0.1,\ \boldsymbol{\varepsilon}_c^w = 1$), while all boundary nodes are fixed.

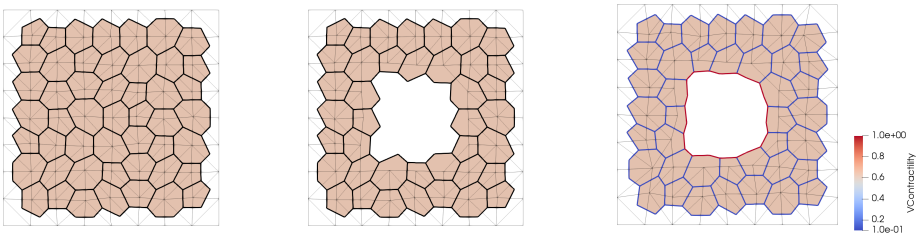

(a) Initial configuration (b) Cell ablation (c) Defromed tissue

Figure 4.3: Manufactured wound healing with prescribed contraction. (a) Initial configuration of cells. (b) Initial configuration with cell ablation. (c) Deformed configuration with fixed boundary nodes. ($k_D = 0.1,\ k_V = 1,\ \lambda_A = 10,\ \lambda_y = 2$)

Then, To check if we can retrieve these contraction, we apply our iterative approach as shown in Figure 4.2, taking only the nodal positions $\boldsymbol{x}$ and wound area A_w^* of the deformed configuration (Figure 4.3(c)) as an input.

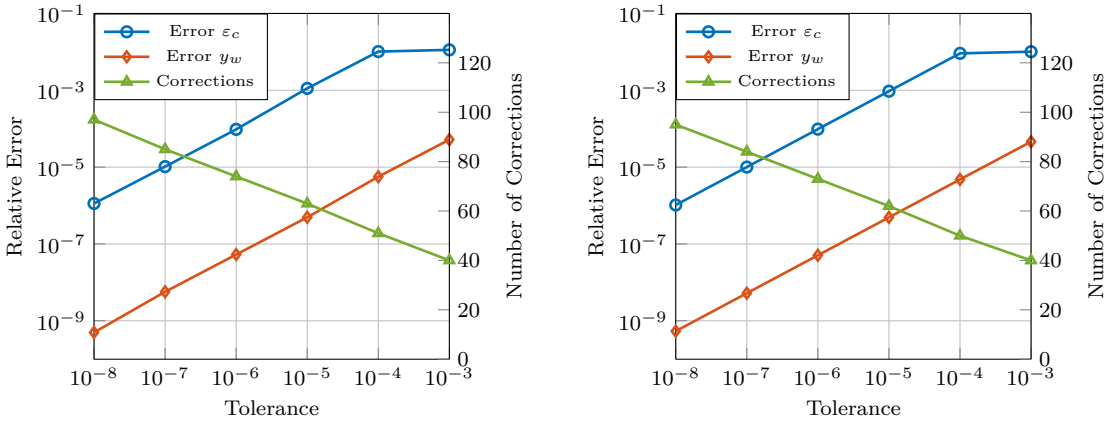

(a) $\lambda_w = 24$ (b) $\lambda_w = 3314$

Figure 4.4: The performance of the iterative approach on manufactured problem. Plots show the relative error (y-axes left) and the number of corrections required to reach convergence (y-axes right) versus the prescribed tolerance in $\boldsymbol{y}_w$-correction.

In Figure 4.4 we plot the relative error associated to the obtained contractions $\boldsymbol{\varepsilon}_c$ as well as wound verices $\boldsymbol{y}_w$, taking different degrees of tolerance (we keep iterating while $tol > \Delta \boldsymbol{y}_w$). As it can be seen the method showed linear convergence regardless of the chosen value of λ_w, while the number of corrections also increases linearly. For this case, different values of λ_w were tested ranging from 10 to 3500, no changes were observed except for ± 5 variation in the number of corrections. In all these tests, similar results were obtained in which the error converges linearly with slop of about 1 for wound vertices and 0.85 for contractility, as for the number of corrections it increase with slop of 11.

4.5.2 Application to Experimental Data

In this section we show the results obtained after applying our methodology on wound healing of embryonic tissue of Drosophila fly. The data is basically a stack of images that were taken by confocal microscopy, these images shows an aggregation of cells after preforming laser ablation on the epithelial structure of the wing disc, with time interval of 30 *second* and dimensions of 500×500 μm, see Figure 4.6(a), 4.6(d), 4.6(g) and 4.6(j).

To extract the position of cell centers $\boldsymbol{x}$ and the wounded are A_w^*, the experimental images had to be preprocessed using various computational algorithms. In particular we used different plugins that are provided by *Fiji* [65] which is a distributions of the image processing program *ImageJ* [66], for more details see Appendix A.

In the beginning, the model was initiated based on the image taken prior to cell ablation ($Time = 0$). Figure 4.5, shows the initial status of the tissue, comparing the boundary of cells obtained by image segmentation with those obtained after applying Delaunay triangulation along with barycenric tessellation using cell centers. As it can be seen, we have considered two different cases, in the first we tessellate taking only cell centers, Figure 4.5(a), while in the second we offset boundary nodes in order to extend our tessellation to include cells on the boundary, Figure 4.5(b). Furthermore, the configurations in Figure 4.5 are assumed to be reference configuration, which means that the initial parameters L_0, A_0 are defined based on them, as well as the connectivity between nodes.

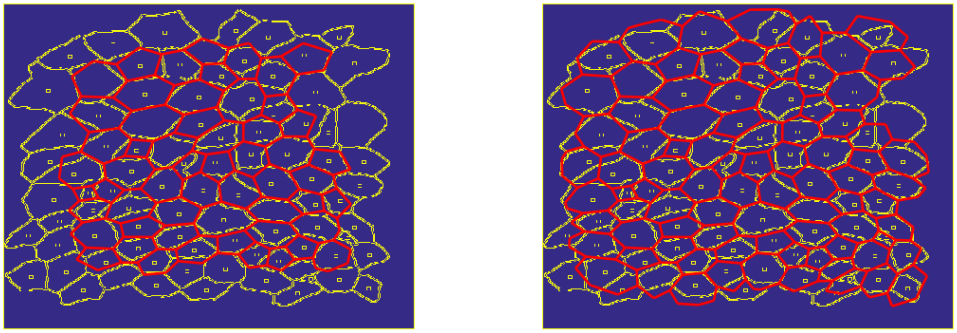

(a) Without boundary offset

(b) With boundary offset

Figure 4.5: The initial configuration of the tissue before call ablation, The yellow represent the true boundary of cells obtained after image segmentation. In red lines is the geometry obtained after applying barycentric tessellation. (a) tessellating with cells centers only. (b) tessellating, after adding offset of boundary nodes.

Then, we preform the procedures illustrated in Figure 4.2 at each time, while in each time step we update only the position of cell centers and wounded area based on the experimental data. In the inverse problem, no assumption were made regarding the boundary conditions instead the equalities corresponding to boundary nodes were excluded. Furthermore, when the tissue is wounded, ablated cells are removed along with the bars coupling them with the neighboring cells, and vertices laying on wound edge are relaxed, see Figure 4.6.

Figure 4.7 and 4.8 shows the obtained evolution of contractions during 15 min after cell ablation. During the time steps that immediately followed cell ablation ($0 < time \leq 7\ min$) we assumed that the tissue is going through an expansion-phase, or in other words the contractions that drives wound closure had not been generated yet, therefore in our inverse problem we are assuming a homogeneous contractility for the whole tissue. Meanwhile for ($time > 7\ min$) we assumed that the tissue had began to heal, thus, we switch to closure-phase in which we solve for two values of contractility, one corresponds to the wound edge while the other is for the rest of the tissue. We remark that the time in which we switch between the two phases ($time = 7\ min$) was chosen empirically based on the observed deformation and the peak value of the wounded area (green plots in Figure 4.7 and 4.8).

During the expansion-phase ($0 < time \leq 7\ min$), it can be seen that value of contractility grows slightly coinciding with increase of wound area (Figure 4.7 and 4.8), however, this growth can be attributed more to the viscoelastic response due to prestresses, rather than cell generated contractions. During closure-phase we observed a dissociation in the values of contracitlity, such that the wound ring took a positive value (contraction), while the rest of the tissue had a negative value (expansion), this outcome arose regardless of the chosen value for the relaxation parameter λ_y.

In this calculation, we observed that the contractility profile is mainly depends on the chosen penalty λ_y on the variation of wounded vertices $\boldsymbol{y}_w$, Figure 4.7 and 4.8 shows the results, while choosing $\lambda_y = \{0.1, 0.5, 1, 5\}$. As it can be seen choosing $\lambda_y \leq 1$ provide a smooth evolution of contraction, while when we choose $\lambda_y > 2$ oscillations start to appear. We report that for $\lambda_y < 1$ instabilities at wound edge (buckling) might be encountered, especially in the time steps which involve considerable change on wounded area, to avoid these collapses one might consider reducing the step size during $\boldsymbol{y}_w$- corrections. In the other hand taking $\lambda_y > 10$ can over constrain vertices and prevent the wound edge from relaxing.

Eventually, the penalty parameter $\boldsymbol{y}_w$ is highly correlated to the viscose effect in cells, since the time step is the same in all cases, the results suggest that wound closure is driven by either a gradual or pulsive increase of contraction, depending on how dominant is the viscose effect in cell structure.

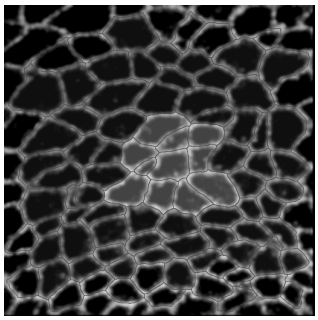

(a) $Time = 0$

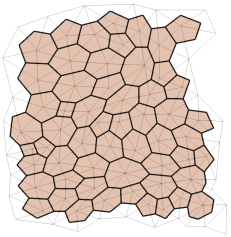

(b) $Time = 0$ (Without offset)

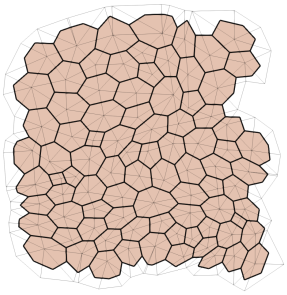

(c) $Time = 0$ (With offset)

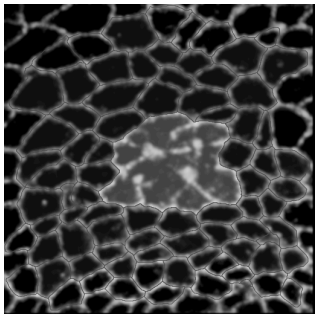

(d) $Time = 0.5\ min$

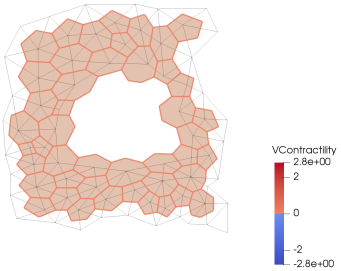

(e) $Time = 0.5$ (Without offset)

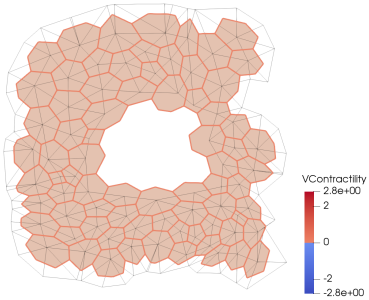

(f) $Time = 0.5$ (With offset)

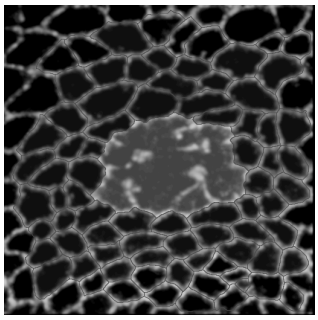

(g) $Time = 9\ min$

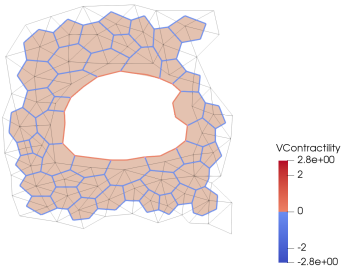

(h) $Time = 9\ min$ (Without offest)

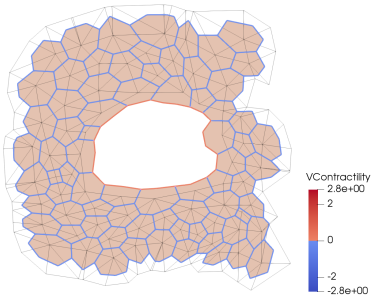

(i) $Time = 0.5\ min$ (With offest)

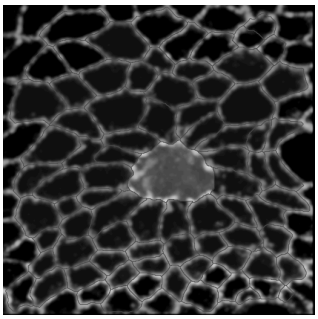

(j) $Time = 14.5\ min$

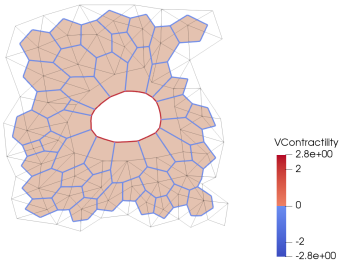

(k) $Time = 14.5\ min$ (Without offest)

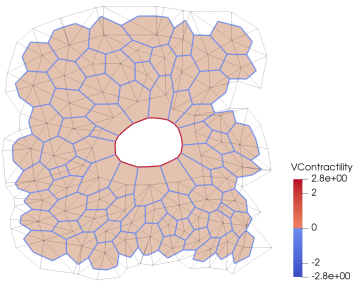

(l) $Time = 0.5\ min$ (With offest)

Figure 4.6: Wound healing at different stages.

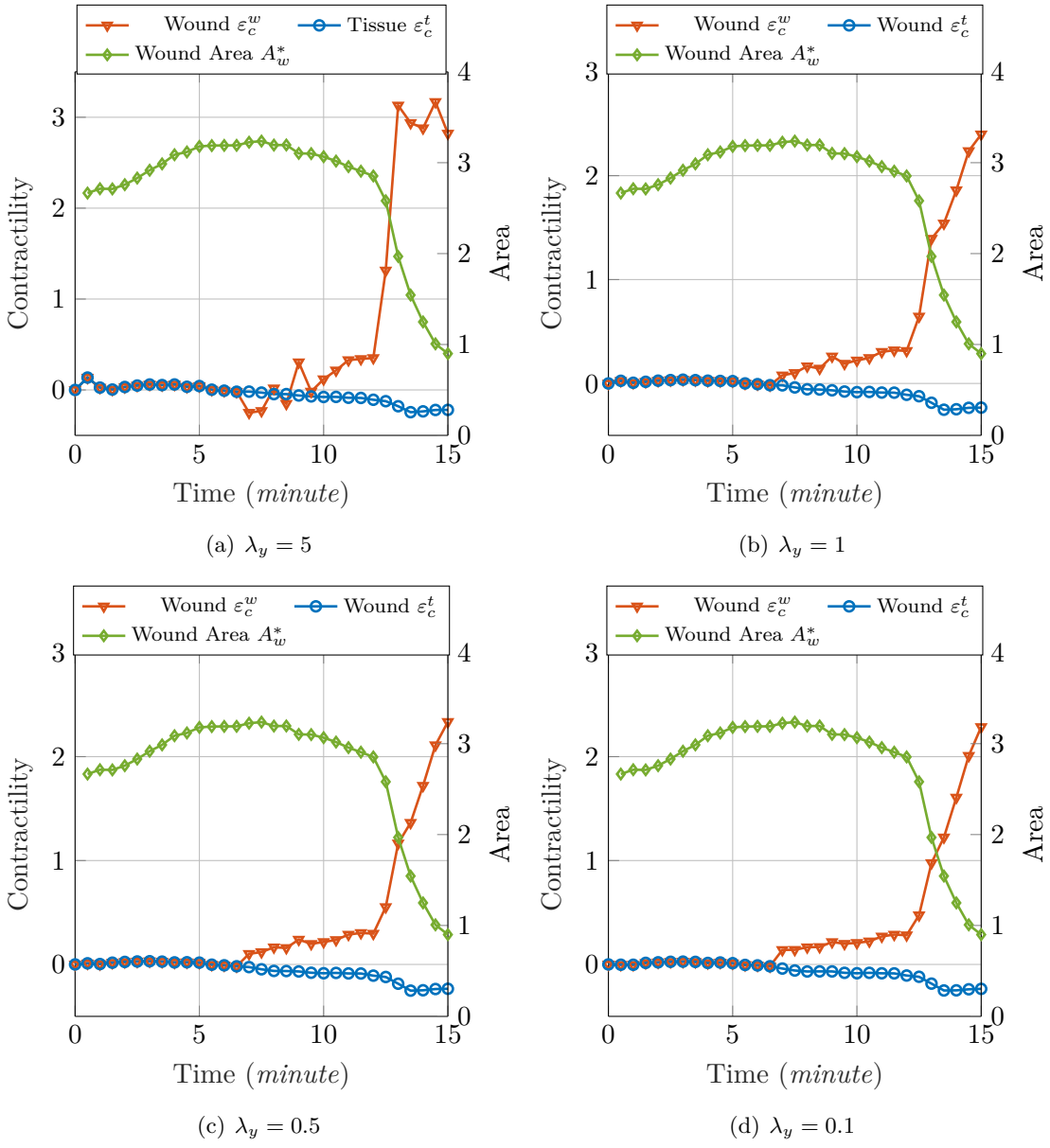

Figure 4.7: Time evolution of cellular contraction during wound healing (y-axes left),with the evolution of true area of wound (y-axes right), **without offset of boundary nodes**. numerical parameter: $k_D = 0.1,\ k_V = 1,\ \lambda_A = 14.14,\ \lambda_w = 14.314$.

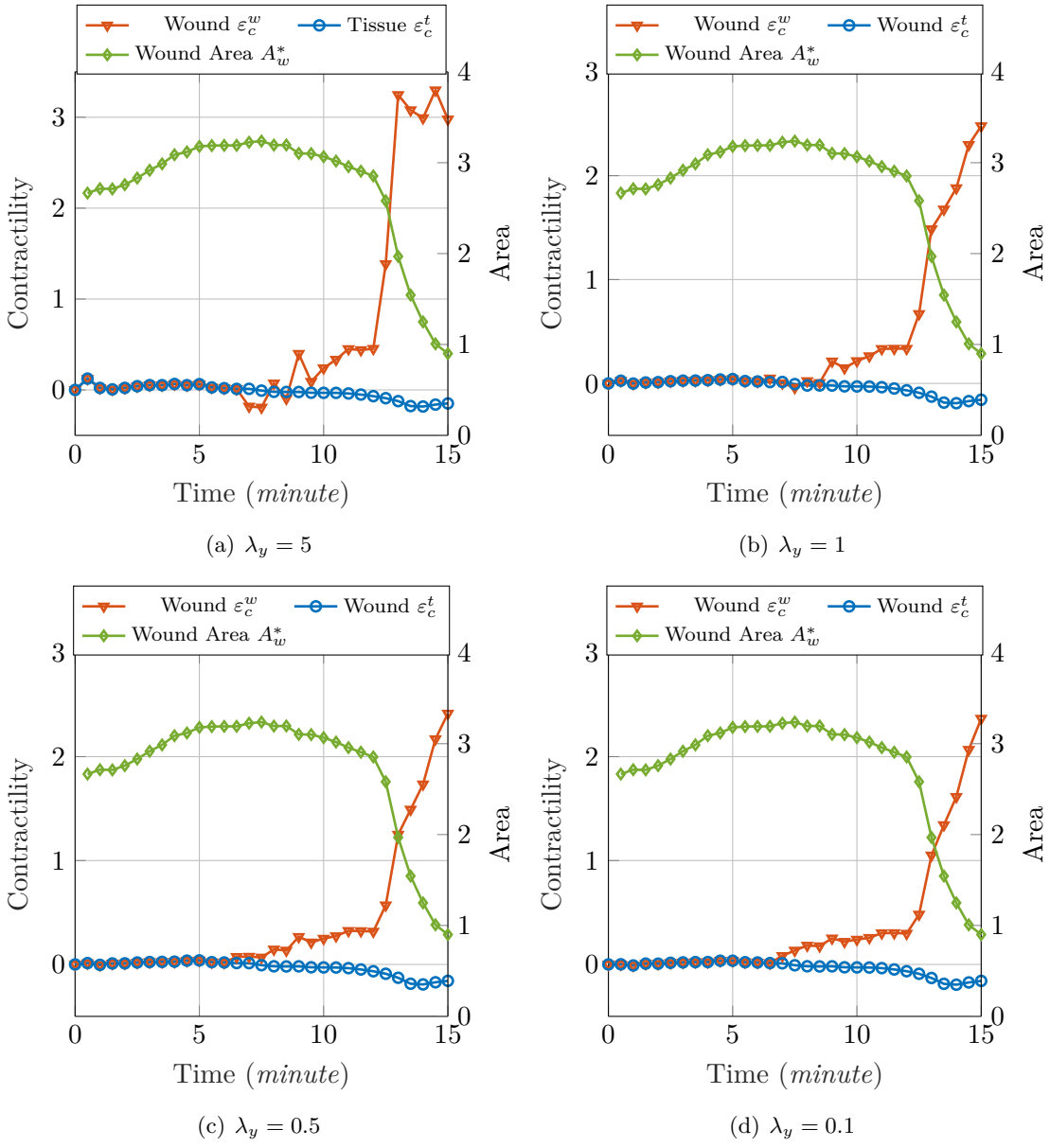

(a) $\lambda_y = 5$ (b) $\lambda_y = 1$

(c) $\lambda_y = 0.5$ (d) $\lambda_y = 0.1$

Figure 4.8: Time evolution of cellular contraction during wound healing (y-axes left),with the evolution of true area of wound (y-axes right), **with offset of boundary nodes**. numerical parameter: $k_D = 0.1,\ k_V = 1,\ \lambda_A = 14.14,\ \lambda_w = 14.314$.

Chapter 5

Conclusion and Future Work

In this work, **a platform for studying both hybrid and purely vertex models has been implemented** in *Matlab R2016a*, with the ability to export and postprocess the results using *Paraview*. Based on the user specification, the implementation can handle both direct and inverse mechanical problems, with an additional branch that is dedicated for **simulating wound healing phenomena**. Furthermore, the models were implemented in such way that it can **incorporate different rheologies** very easily, by changing only the expression for the traction eq.(2.16) and their derivatives.

We have preformed **inverse analysis on hybrid vertex model** to infer cellular contractions on epithelial tissues. We have found that the inverse mechanical problem do have a solution, however, uniqueness can not be guaranteed, while regularizing might be a practical approach, we have found that there are **many sets of contractions that can produce the same deformation**. Nevertheless, in future work, this non-uniqueness of the solution might be an advantage when we consider an inverse problem for a sequential set of deformations, such that one might pick the solution which minimizes the discontinuity between these deformations. Moreover, it was observed that the reactions on **the boundary of the tissue plays a crucial role** on the obtained value of contractility, which proposes considering the possibility of introducing and an elastic boundary such that one might approximate these reactions form an observed deformation.

We have extended our analysis to include **purely vertex** model, in which we found that for most of the cases **mechanical equilibrium is invertible with a unique** solution, while **infeasibility might be encountered in the direct problem**. One common way to overcome this problem is considered an explicit dissipative forces that acts on vertices [38] [45].

We have applied our implementation to infer the contraction during the **wound healing of embryonic tissue of Drosophila fly**. It was found that the pattern in which the **wound ring contracts depends highly on the level of the viscose effect**. This observation might be investigated in future work, considering more realistic rheology with appropriate numerical parameter. Also, future work should be devoted to include **tissue remodeling**, which is the main limitation of the current work.

Appendices

Appendix A

Image Processing

In this work various computational algorithms were used to extract data from experimental images, in particular we used different plugins that are provided by Fiji [65] which is a distributions of the image processing program ImageJ [66]. First, the images were segmented using a watershed algorithm called Morphological Segmentation [67], which allows to define the boundary of cells, see Figure A.1-(b). Then, we used Particle Analysis in order to measure the dimension of each cell, Particle Analysis is built-in tool that can distinguish closed objects from its surrounding, which was found handy in obtaining the area of wound and cells as well as their centroids, see Figur A.1-(c). The next step involved writing a simple script in ImageJ Macro language which basically reads and plots the centroids of each cell, see Figure A.1-(d). As final step, we used another plugin of Fiji called TrackMate [68], such that from the stack of images in which cell centers are marked, TrackMate provides segregated trajectories which describe how cell centroids changes over time, see Figure A.1-(e)

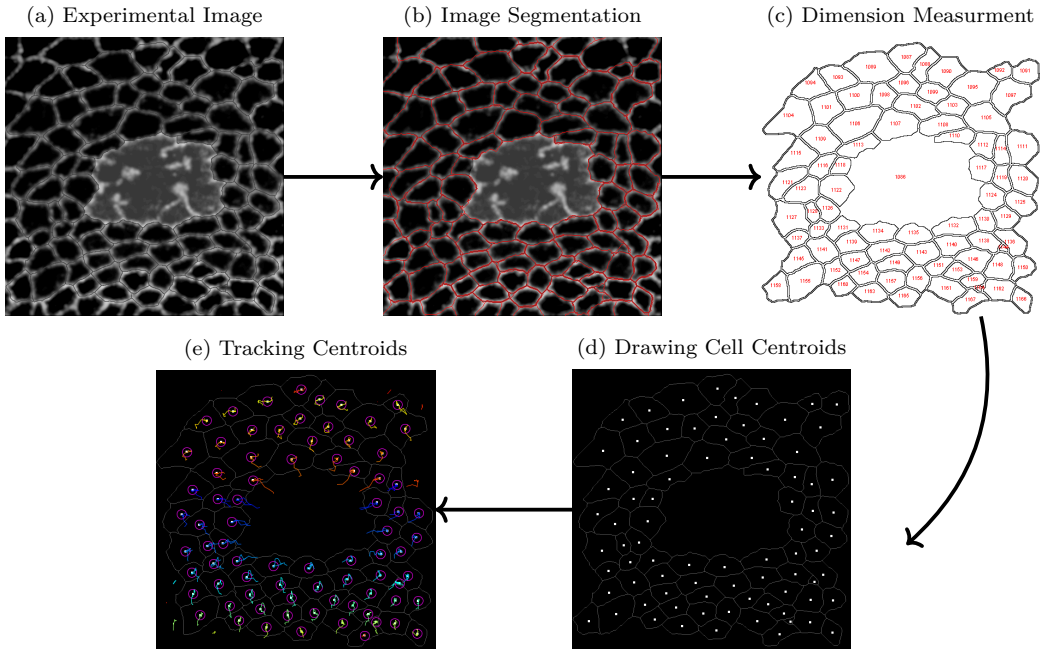

Figure A.1: Illustration of the methods used to extract the trajectory of cell centers during wound healing. (a) Input example of confocal images of a wounded monolyer. (b) Indicating cell junctions using Morphological Segmentation. (c) Measuring cell dimensions with Particle Analysis. (d) Drawing the center of area of each cell. (e) Tracking the centroids of cells with TrackMate.

Bibliography

[1] Tadanori Mammoto, Akiko Mammoto, and Donald E. Ingber. "Mechanobiology and Developmental Control". In: *Annual Review of Cell and Developmental Biology* 29.1 (2013). PMID: 24099083, pp. 27–61. DOI: 10.1146/annurev-cellbio-101512-122340. eprint: https://doi.org/10.1146/annurev-cellbio-101512-122340. URL: https://doi.org/10.1146/annurev-cellbio-101512-122340.

[2] Agustí Brugués et al. "Forces driving epithelial wound healing". In: *Nature physics*. 2014.

[3] Nicolas C. Rivron et al. "Tissue deformation spatially modulates VEGF signaling and angiogenesis". In: *Proceedings of the National Academy of Sciences* 109.18 (2012), pp. 6886–6891. ISSN: 0027-8424. DOI: 10.1073/pnas.1201626109. eprint: http://www.pnas.org/content/109/18/6886.full.pdf. URL: http://www.pnas.org/content/109/18/6886.

[4] Denis Wirtz, Konstantinos Konstantopoulos, and Peter C. Searson. "The physics of cancer: the role of physical interactions and mechanical forces in metastasis". In: *Nature Reviews Cancer* 11 (2011), pp. 512–522.

[5] Xavier Trepat et al. "Physical forces during collective cell migration". In: *Nature Physics* 5 (2009). Times Cited: 162, pp. 426–430.

[6] Carl-Philipp Heisenberg and Yohanns Bellaïche. "Forces in Tissue Morphogenesis and Patterning". In: *Cell* 153 (2013), pp. 948–962.

[7] Pilot Fanny and Lecuit Thomas. "Compartmentalized morphogenesis in epithelia: From cell to tissue shape". In: *Developmental Dynamics* 232.3 (), pp. 685–694. DOI: 10.1002/dvdy.20334. eprint: https://onlinelibrary.wiley.com/doi/pdf/10.1002/dvdy.20334. URL: https://onlinelibrary.wiley.com/doi/abs/10.1002/dvdy.20334.

[8] Raju Tomer et al. "Quantitative high-speed imaging of entire developing embryos with simultaneous multiview light-sheet microscopy". In: *Nat Meth* 9.7 (July 2012), pp. 755–763. ISSN: 15487091. URL: http://dx.doi.org/10.1038/nmeth.2062.

[9] Adam C. Martin et al. "Integration of contractile forces during tissue invagination". In: *The Journal of Cell Biology* 188.5 (2010), pp. 735–749. ISSN: 0021-9525. DOI: 10.1083/jcb.200910099. eprint: http://jcb.rupress.org/content/188/5/735.full.pdf. URL: http://jcb.rupress.org/content/188/5/735.

[10] Jungbauer Simon et al. “Cell Shape Normalization, Dendrite Orientation, and Melanin Production of Normal and Genetically Altered (Haploinsufficient NF1)Melanocytes by Microstructured Substrate Interactions”. In: *ChemPhysChem* 5.1 (), pp. 85–92. DOI: 10.1002/cphc.200300868. eprint: https://onlinelibrary.wiley.com/doi/pdf/10.1002/cphc.200300868. URL: https://onlinelibrary.wiley.com/doi/abs/10.1002/cphc.200300868.

[11] Adam J. Engler et al. “Matrix Elasticity Directs Stem Cell Lineage Specification”. In: *Cell* 126.4 (2006), pp. 677–689. ISSN: 0092-8674. DOI: https://doi.org/10.1016/j.cell.2006.06.044. URL: http://www.sciencedirect.com/science/article/pii/S0092867406009615.

[12] Tadanori Mammoto and Donald E. Ingber. “Mechanical control of tissue and organ development”. In: *Development* 137.9 (2010), pp. 1407–1420. ISSN: 0950-1991. DOI: 10.1242/dev.024166. eprint: http://dev.biologists.org/content/137/9/1407.full.pdf. URL: http://dev.biologists.org/content/137/9/1407.

[13] Michele A Wozniak and Christopher S Chen. “Mechanotransduction in development: a growing role for contractility”. In: *Nature reviews. Molecular cell biology* 10.1 (Jan. 2009), pp. 34–43. ISSN: 1471-0072. DOI: 10.1038/nrm2592. URL: http://europepmc.org/articles/PMC2952188.

[14] Jochen Guck and Edwin R. Chilvers. “Mechanics Meets Medicine”. In: *Science Translational Medicine* 5.212 (2013), 212fs41–212fs41. ISSN: 1946-6234. DOI: 10.1126/scitranslmed.3007731. eprint: http://stm.sciencemag.org/content/5/212/212fs41.full.pdf. URL: http://stm.sciencemag.org/content/5/212/212fs41.

[15] Xavier Trepat, Guillaume Lenormand, and Jeffrey J. Fredberg. “Universality in cell mechanics”. In: *Soft Matter* 4 (9 2008), pp. 1750–1759. DOI: 10.1039/B804866E. URL: http://dx.doi.org/10.1039/B804866E.

[16] M. L. Gardel et al. “Elastic Behavior of Cross-Linked and Bundled Actin Networks”. In: *Science* 304.5675 (2004), pp. 1301–1305. ISSN: 0036-8075. DOI: 10.1126/science.1095087. eprint: http://science.sciencemag.org/content/304/5675/1301.full.pdf. URL: http://science.sciencemag.org/content/304/5675/1301.

[17] P. Bursac et al. “Cytoskeletal remodelling and slow dynamics in the living cell”. In: *Nature Materials* 4 (2005), pp. 557–561.

[18] Guillaume Lenormand et al. “Out-of-equilibrium dynamics in the cytoskeleton of the living cell”. In: *Phys. Rev. E* 76 (4 Oct. 2007), p. 041901. DOI: 10.1103/PhysRevE.76.041901. URL: https://link.aps.org/doi/10.1103/PhysRevE.76.041901.

[19] José J Muñoz, David Amat, and Vito Conte. “Computation of forces from deformed visco-elastic biological tissues”. In: *Inverse Problems* 34.4 (2018), p. 044001. URL: http://stacks.iop.org/0266-5611/34/i=4/a=044001.

[20] Yousef Jamali, Mohammad Azimi, and Mohammad R. K. Mofrad. "A Sub-Cellular Viscoelastic Model for Cell Population Mechanics". In: *PLOS ONE* 5.8 (Aug. 2010), pp. 1–20. DOI: 10.1371/journal.pone.0012097. URL: https://doi.org/10.1371/journal.pone.0012097.

[21] N. Asadipour, X. Trepat, and J.J. Muñoz. "Porous-based rheological model for tissue fluidisation". In: *Journal of the Mechanics and Physics of Solids* 96 (2016), pp. 535–549. ISSN: 0022-5096. DOI: https://doi.org/10.1016/j.jmps.2016.07.002. URL: http://www.sciencedirect.com/science/article/pii/S0022509616301260.

[22] J. Howard. "Mechanics of motor proteins". In: *Physics of bio-molecules and cells. Physique des biomolécules et des cellules*. Ed. by F. Flyvbjerg et al. Berlin, Heidelberg: Springer Berlin Heidelberg, 2002, pp. 69–94. ISBN: 978-3-540-45701-5.

[23] Thomas Lecuit, Pierre-François Lenne, and Edwin Munro. "Force Generation, Transmission, and Integration during Cell and Tissue Morphogenesis". In: *Annual Review of Cell and Developmental Biology* 27.1 (2011). PMID: 21740231, pp. 157–184. DOI: 10.1146/annurev-cellbio-100109-104027. eprint: https://doi.org/10.1146/annurev-cellbio-100109-104027. URL: https://doi.org/10.1146/annurev-cellbio-100109-104027.

[24] Lance A. Davidson et al. "Emergent morphogenesis: Elastic mechanics of a self-deforming tissue". In: *Journal of Biomechanics* 43.1 (2010). Special Issue on Cell Mechanobiology, pp. 63–70. ISSN: 0021-9290. DOI: https://doi.org/10.1016/j.jbiomech.2009.09.010. URL: http://www.sciencedirect.com/science/article/pii/S0021929009005016.

[25] Wyczalkowski Matthew A. et al. "Computational models for mechanics of morphogenesis". In: *Birth Defects Research Part C: Embryo Today: Reviews* 96.2 (), pp. 132–152. DOI: 10.1002/bdrc.21013. eprint: https://onlinelibrary.wiley.com/doi/pdf/10.1002/bdrc.21013. URL: https://onlinelibrary.wiley.com/doi/abs/10.1002/bdrc.21013.

[26] Edouard Hannezo, Jacques Prost, and Jean-Fran çois Joanny. "Mechanical Instabilities of Biological Tubes". In: *Phys. Rev. Lett.* 109 (1 July 2012), p. 018101. DOI: 10.1103/PhysRevLett.109.018101. URL: https://link.aps.org/doi/10.1103/PhysRevLett.109.018101.

[27] José J. Muñoz, Kathy Barrett, and Mark Miodownik. "A deformation gradient decomposition method for the analysis of the mechanics of morphogenesis". In: *Journal of Biomechanics* 40.6 (2007), pp. 1372–1380. ISSN: 0021-9290. DOI: https://doi.org/10.1016/j.jbiomech.2006.05.006. URL: http://www.sciencedirect.com/science/article/pii/S0021929006001631.

[28] Vito Conte, José J Muñoz, and Mark Miodownik. "A 3D finite element model of ventral furrow invagination in the Drosophila melanogaster embryo". In: *Journal of the Mechanical Behavior of Biomedical Materials* 1.2 (2008), pp. 188–198. ISSN:

1751-6161. DOI: https://doi.org/10.1016/j.jmbbm.2007.10.002. URL: http://www.sciencedirect.com/science/article/pii/S175161610700032X.

[29] Andreas Menzel and Ellen Kuhl. "Frontiers in growth and remodeling". In: *Mechanics Research Communications* 42 (2012). Recent Advances in the Biomechanics of Growth and Remodeling, pp. 1–14. ISSN: 0093-6413. DOI: https://doi.org/10.1016/j.mechrescom.2012.02.007. URL: http://www.sciencedirect.com/science/article/pii/S0093641312000225.

[30] G. Wayne Brodland, Denis Viens, and Jim H. Veldhuis. "A new cell-based FE model for the mechanics of embryonic epithelia". In: *Computer Methods in Biomechanics and Biomedical Engineering* 10.2 (2007). PMID: 18651278, pp. 121–128. DOI: 10.1080/10255840601124704. eprint: https://doi.org/10.1080/10255840601124704. URL: https://doi.org/10.1080/10255840601124704.

[31] Y. Lee et al. "A cellular automaton model for the proliferation of migrating contact-inhibited cells". In: *Biophysical Journal* 69 (Oct. 1995), pp. 1284–1298. DOI: 10.1016/S0006-3495(95)79996-9.

[32] M. Block, E. Schöll, and D. Drasdo. "Classifying the Expansion Kinetics and Critical Surface Dynamics of Growing Cell Populations". In: *Phys. Rev. Lett.* 99 (24 Dec. 2007), p. 248101. DOI: 10.1103/PhysRevLett.99.248101. URL: https://link.aps.org/doi/10.1103/PhysRevLett.99.248101.

[33] Michael Krieg et al. "Tensile forces govern germ-layer organization in zebrafish". In: *Nature Cell Biology* 10 (2008), pp. 429–436.

[34] Jos Käfer et al. "Cell adhesion and cortex contractility determine cell patterning in the Drosophilaretina". In: *Proceedings of the National Academy of Sciences* 104.47 (2007), pp. 18549–18554. ISSN: 0027-8424. DOI: 10.1073/pnas.0704235104. eprint: http://www.pnas.org/content/104/47/18549.full.pdf. URL: http://www.pnas.org/content/104/47/18549.

[35] Silvanus Alt, Poulami Ganguly, and Guillaume Salbreux. "Vertex models: from cell mechanics to tissue morphogenesis". In: *Philosophical transactions of the Royal Society of London. Series B, Biological sciences*. 2017.

[36] Alexander G. Fletcher et al. "Vertex Models of Epithelial Morphogenesis". In: *Biophysical Journal* 106.11 (2014), pp. 2291–2304. ISSN: 0006-3495. DOI: https://doi.org/10.1016/j.bpj.2013.11.4498. URL: http://www.sciencedirect.com/science/article/pii/S0006349513057949.

[37] Lars Hufnagel et al. "On the mechanism of wing size determination in fly development". In: *Proceedings of the National Academy of Sciences* 104.10 (2007), pp. 3835–3840. ISSN: 0027-8424. DOI: 10.1073/pnas.0607134104. eprint: http://www.pnas.org/content/104/10/3835.full.pdf. URL: http://www.pnas.org/content/104/10/3835.

[38] Shao-Zhen Lin, Bo Li, and Xi-Qiao Feng. "A dynamic cellular vertex model of growing epithelial tissues". In: *Acta Mechanica Sinica* 33.2 (Apr. 2017), pp. 250–259. ISSN: 1614-3116. DOI: 10.1007/s10409-017-0654-y. URL: https://doi.org/10.1007/s10409-017-0654-y.

[39] Ana Hoevar Brezavek et al. "A model of epithelial invagination driven by collective mechanics of identical cells". In: *Biophysical journal* 103.5 (Sept. 2012), pp. 1069–1077. ISSN: 0006-3495. DOI: 10.1016/j.bpj.2012.07.018. URL: http://europepmc.org/articles/PMC3433605.

[40] Philipp Spahn and Rolf Reuter. "A Vertex Model of Drosophila Ventral Furrow Formation". In: *PLOS ONE* 8.9 (Sept. 2013), pp. 1–15. DOI: 10.1371/journal.pone.0075051. URL: https://doi.org/10.1371/journal.pone.0075051.

[41] Tatsuzo Nagai and Hisao Honda. "Computer simulation of wound closure in epithelial tissues: Cell–basal-lamina adhesion". In: *Phys. Rev. E* 80 (6 Dec. 2009), p. 061903. DOI: 10.1103/PhysRevE.80.061903. URL: https://link.aps.org/doi/10.1103/PhysRevE.80.061903.

[42] Payman Mosaffa, A. Rodríguez-Ferran, and Jose J. Muñoz. "Hybrid cell-centred/vertex model for multicellular systems with equilibrium-preserving remodelling." In: *International journal for numerical methods in biomedical engineering* 34 3 (2018).

[43] Guillaume Salbreux et al. "Coupling Mechanical Deformations and Planar Cell Polarity to Create Regular Patterns in the Zebrafish Retina". In: *PLOS Computational Biology* 8.8 (Aug. 2012), pp. 1–20. DOI: 10.1371/journal.pcbi.1002618. URL: https://doi.org/10.1371/journal.pcbi.1002618.

[44] D. B. Staple et al. "Mechanics and remodelling of cell packings in epithelia". In: *The European Physical Journal E* 33.2 (Oct. 2010), pp. 117–127. ISSN: 1292-895X. DOI: 10.1140/epje/i2010-10677-0. URL: https://doi.org/10.1140/epje/i2010-10677-0.

[45] Alexander G. Fletcher et al. "Implementing vertex dynamics models of cell populations in biology within a consistent computational framework". In: *Progress in Biophysics and Molecular Biology* 113.2 (2013), pp. 299–326. ISSN: 0079-6107. DOI: https://doi.org/10.1016/j.pbiomolbio.2013.09.003. URL: http://www.sciencedirect.com/science/article/pii/S0079610713000989.

[46] Ben Fabry et al. "Scaling the Microrheology of Living Cells". In: *Phys. Rev. Lett.* 87 (14 Sept. 2001), p. 148102. DOI: 10.1103/PhysRevLett.87.148102. URL: https://link.aps.org/doi/10.1103/PhysRevLett.87.148102.

[47] Sylvie Hénon et al. "A New Determination of the Shear Modulus of the Human Erythrocyte Membrane Using Optical Tweezers". In: *Biophysical Journal* 76.2 (1999), pp. 1145–1151. ISSN: 0006-3495. DOI: https://doi.org/10.1016/S0006-3495(99)77279-6. URL: http://www.sciencedirect.com/science/article/pii/S0006349599772796.

[48] Andrew R. Harris et al. “Characterizing the mechanics of cultured cell monolayers”. In: *Proceedings of the National Academy of Sciences* 109.41 (2012), pp. 16449–16454. ISSN: 0027-8424. DOI: 10.1073/pnas.1213301109. eprint: http://www.pnas.org/content/109/41/16449.full.pdf. URL: http://www.pnas.org/content/109/41/16449.

[49] Andrew R. Harris et al. “Generating suspended cell monolayers for mechanobiological studies”. In: *Nature Protocols* 8 (2013), pp. 2516–2530.

[50] DANIEL J. MÜLLER and YVES F. DUFRÊNE. “Atomic force microscopy as a multifunctional molecular toolbox in nanobiotechnology”. In: *Nanoscience and Technology*, pp. 269–277. DOI: 10.1142/9789814287005_0028. eprint: https://www.worldscientific.com/doi/pdf/10.1142/9789814287005_0028. URL: https://www.worldscientific.com/doi/abs/10.1142/9789814287005_0028.

[51] G Vitale, L Preziosi, and D Ambrosi. “A numerical method for the inverse problem of cell traction in 3D”. In: *Inverse Problems* 28.9 (2012), p. 095013. URL: http://stacks.iop.org/0266-5611/28/i=9/a=095013.

[52] Xavier Serra-Picamal et al. “Chapter 17 - Mapping forces and kinematics during collective cell migration”. In: *Biophysical Methods in Cell Biology*. Ed. by Ewa K. Paluch. Vol. 125. Methods in Cell Biology. Academic Press, 2015, pp. 309–330. DOI: https://doi.org/10.1016/bs.mcb.2014.11.003. URL: http://www.sciencedirect.com/science/article/pii/S0091679X14000375.

[53] Jianping Fu et al. “Mechanical regulation of cell function with geometrically modulated elastomeric substrates”. In: *Nature methods* 7.9 (Sept. 2010), pp. 733–736. ISSN: 1548-7091. DOI: 10.1038/nmeth.1487. URL: http://europepmc.org/articles/PMC3069358.

[54] Catherine G Galbraith and Michael P Sheetz. “A micromachined device provides a new bend on fibroblast traction forces.” In: *Proceedings of the National Academy of Sciences of the United States of America* 94 17 (1997), pp. 9114–8.

[55] José J Muñoz, David Amat, and Vito Conte. “Computation of forces from deformed visco-elastic biological tissues”. In: *Inverse Problems* 34.4 (2018), p. 044001. URL: http://stacks.iop.org/0266-5611/34/i=4/a=044001.

[56] Kevin K. Chiou, Lars Hufnagel, and Boris I. Shraiman. “Mechanical Stress Inference for Two Dimensional Cell Arrays”. In: *PLOS Computational Biology* 8.5 (May 2012), pp. 1–9. DOI: 10.1371/journal.pcbi.1002512. URL: https://doi.org/10.1371/journal.pcbi.1002512.

[57] G. Wayne Brodland et al. “Video force microscopy reveals the mechanics of ventral furrow invagination in Drosophila”. In: *Proceedings of the National Academy of Sciences* 107.51 (2010), pp. 22111–22116. ISSN: 0027-8424. DOI: 10.1073/pnas.1006591107. eprint: http://www.pnas.org/content/107/51/22111.full.pdf. URL: http://www.pnas.org/content/107/51/22111.

[58] P. Graham Cranston et al. “Cinemechanometry (CMM): A Method to Determine the Forces that Drive Morphogenetic Movements from Time-Lapse Images”. In: *Annals of Biomedical Engineering* 38.9 (Sept. 2010), pp. 2937–2947. ISSN: 1573-9686. DOI: 10.1007/s10439-010-9998-1. URL: https://doi.org/10.1007/s10439-010-9998-1.

[59] G. Wayne Brodland et al. “CellFIT: A Cellular Force-Inference Toolkit Using Curvilinear Cell Boundaries”. In: *PLOS ONE* 9.6 (June 2014), pp. 1–15. DOI: 10.1371/journal.pone.0099116. URL: https://doi.org/10.1371/journal.pone.0099116.

[60] Jim H. Veldhuis et al. “Inferring cellular forces from image stacks”. In: *Philosophical Transactions of the Royal Society of London B: Biological Sciences* 372.1720 (2017). ISSN: 0962-8436. DOI: 10.1098/rstb.2016.0261. eprint: http://rstb.royalsocietypublishing.org/content/372/1720/20160261.full.pdf. URL: http://rstb.royalsocietypublishing.org/content/372/1720/20160261.

[61] Payman Mosaffa. “Hybrid Cell-centred/Vertex Model for Multicellular Systems”. PhD thesis. Universitat Politecnica de Catalunya, 2014.

[62] C. Bradford Barber, David P. Dobkin, and Hannu Huhdanpaa. “The Quickhull Algorithm for Convex Hulls”. In: *ACM Trans. Math. Softw.* 22.4 (Dec. 1996), pp. 469–483. ISSN: 0098-3500. DOI: 10.1145/235815.235821. URL: http://doi.acm.org/10.1145/235815.235821.

[63] Michael Grant and Stephen Boyd. *CVX: Matlab Software for Disciplined Convex Programming, version 2.1*. http://cvxr.com/cvx. Mar. 2014.

[64] Maria Teresa Abreu-Blanco et al. “Drosophila embryos close epithelial wounds using a combination of cellular protrusions and an actomyosin purse string”. In: *Journal of Cell Science* 125.24 (2012), pp. 5984–5997. ISSN: 0021-9533. DOI: 10.1242/jcs.109066. eprint: http://jcs.biologists.org/content/125/24/5984.full.pdf. URL: http://jcs.biologists.org/content/125/24/5984.

[65] Johannes Schindelin et al. “Fiji: an open-source platform for biological-image analysis”. In: *Nature Methods*. Nature Methods 9.7 (2012), pp. 676–682. ISSN: 1548-7091. DOI: 10.1038/nmeth.2019. URL: http://www.zora.uzh.ch/id/eprint/75354/.

[66] Curtis T. Rueden et al. “ImageJ2: ImageJ for the next generation of scientific image data”. In: *BMC Bioinformatics* 18.1 (Nov. 2017), p. 529. ISSN: 1471-2105. DOI: 10.1186/s12859-017-1934-z. URL: https://doi.org/10.1186/s12859-017-1934-z.

[67] David Legland, Ignacio Arganda-Carreras, and Philippe Andrey. “MorphoLibJ: integrated library and plugins for mathematical morphology with ImageJ”. In: *Bioinformatics* 32.22 (2016), pp. 3532–3534. DOI: 10.1093/bioinformatics/btw413. eprint: /oup/backfile/content_public/journal/bioinformatics/32/22/10.1093_bioinformatics_btw413/3/btw413.pdf. URL: http://dx.doi.org/10.1093/bioinformatics/btw413.

[68] Jean-Yves Tinevez et al. “TrackMate: An open and extensible platform for single-particle tracking”. In: *Methods* 115 (2017). Image Processing for Biologists, pp. 80–90. ISSN: 1046-2023. DOI: https://doi.org/10.1016/j.ymeth.2016.09.016. URL: http://www.sciencedirect.com/science/article/pii/S1046202316303346.